PHYSIOLOGY

Lactate transported by MCT1 plays an active role in promoting mitochondrial biogenesis and enhancing TCA flux in skeletal muscle

Lingling Zhang†, Chenhao Xin†, Shuo Wang, Shixuan Zhuo, Jing Zhu, Zi Li, Yuyi Liu, Lifeng Yang*, Yan Chen*

Once considered as a "metabolic waste," lactate is now recognized as a major fuel for tricarboxylic acid (TCA) cycle. Our metabolic flux analysis reveals that skeletal muscle mainly uses lactate to fuel TCA cycle. Lactate is transported through the cell membrane via monocarboxylate transporters (MCTs) in which MCT1 is highly expressed in the muscle. We analyzed how MCT1 affects muscle functions using mice with specific deletion of MCT1 in skeletal muscle. MCT1 deletion enhances running performance, increases oxidative fibers while decreasing glycolytic fibers, and enhances flux of glucose to TCA cycle. MCT1 deficiency increases the expression of mitochondrial proteins, augments cell respiration rate, and elevates mitochondrial activity in the muscle. Mechanistically, the protein level of PGC-1α, a master regulator of mitochondrial biogenesis, is elevated upon loss of MCT1 via increases in cellular NAD^+ level and SIRT1 activity. Collectively, these results demonstrate that MCT1-mediated lactate shuttle plays a key role in regulating muscle functions by modulating mitochondrial biogenesis and TCA flux.

INTRODUCTION

As the end product of glycolysis, lactate has been the center of controversy in biology and exercise physiology (*1*). Lactate was originally discovered by Swedish apothecary and chemist Carl Wilhelm Scheele in 1780 in sour milk. Within the physiological pH range in the body, lactate is more than 99% dissociated into lactate anions (La^-) and protons (H^+). For over 200 years and even up to now, lactate was arguably considered "metabolic waste" in "the muscles of hunted age" causing fatigue and muscle soreness. This paradigm was mainly formed in early days by experiments showing "hypoxia/anoxia (low O_2) evokes high lactate" and vice versa "high lactate denotes low O_2" (*1*). The discoveries that skeletal muscle and many other tissues/cells can produce lactate under fully aerobic conditions led George Brooks to propose a "lactate shuttle" theory in the mid-1980s (*2*, *3*). The core of the lactate shuttle theory holds that lactate is an energy intermediate that is formed in cells/tissues with high glycolytic activity and then consumed by cells/tissues with high oxidative activity (*3*, *4*). Lactate is now considered an important energy source for oxidative phosphorylation in cells/tissues, such as oxidative muscle fibers, as well as a precursor for gluconeogenesis (in the liver) and glycogenesis (in liver and skeletal muscle) (*1*, *4*). The importance of lactate as an energy source was highlighted by a recent discovery with flux analysis illustrating that lactate is a preferred fuel feeding the TCA cycle to glucose (*5*, *6*). This finding supports earlier proposals that intracellular lactate shuttle is involved in the utilization of lactate as a fuel for TCA cycle via mitochondria lactate oxidation complex (mLOC) (*3*, *7*, *8*). In addition to serving as a fuel source, lactate can initiate signaling cascade in certain cells upon binding to membrane receptors, exemplified by the discovery that lactate inhibits lipolysis of adipocytes via membrane hydroxycarboxylic acid receptor 1 receptor (*9*). Lately, lactate was found to execute epigenetic regulation on gene expression through lactylation of histone and thereby regulate macrophage functions (*10*).

Cell-cell and intracellular communication of lactate can be accomplished by membrane transporters. A series of work mainly in the Halestrap laboratory discovered that the transmembrane movement of lactate is carried out by members of the solute carrier family 16 (SLC16) (*11*). Within this family, monocarboxylate transporters (MCTs) 1 to 4 (encoded by *Slc16a1*, *Slc16a7*, *Slc16a8*, and *Slc16a3*, respectively) are responsible for transport of lactate, pyruvate, and ketone bodies. MCT-mediated monocarboxylate transport is concentration dependent, adenosine triphosphate (ATP) independent, saturable, stereospecific, competitively inhibited by other monocarboxylates, sensitive to temperature, and stimulated by $[H^+]$ gradients (*1*). MCT1, first cloned in 1994, has the broadest expression among MCTs 1 to 4 and is often highly expressed in cells with high oxidative activity, such as oxidative muscle fibers (*12*–*14*). MCT1 was also found in the mitochondria of cardiac and skeletal muscle (*15*). MCT4 expression is also correlated with high glycolytic activity of the skeletal muscle (*13*, *16*). In addition, MCT2 has little expression in skeletal muscle (*17*), while MCT3 is restricted to the basal membrane of retinal pigment epithelium and choroid plexus epithelium (*1*).

Recently, human mutation studies and mouse models with disruption of genes involved in lactate transporters have aided in elucidating the physiological and pathophysiological functions of lactate transport in a tissue-specific manner, thereby highlighting MCT1 as an important player in numerous physiological processes and diseases. Inactivation of MCT1 caused by mutations leads to defective utilization of ketone bodies and consequently results in recurrent ketoacidosis in children (*18*). Homozygous MCT1 deletion ($Slc16a1^{-/-}$) in mice led to embryonic lethality, while the haploinsufficient mice ($Slc16a1^{+/-}$) were resistant to diet-induced obesity and associated metabolic perturbations (*19*). Studies with heterozygous $Slc16a1^{+/-}$ mice also indicated the role of MCT1 in the regulation of pH homeostasis and cellular energy homeostasis

CAS Key Laboratory of Nutrition, Metabolism and Food Safety, Shanghai Institute of Nutrition and Health, University of Chinese Academy of Sciences, Chinese Academy of Sciences, Shanghai, China, 200031.
*Corresponding author. Email: ychen3@sibs.ac.cn (Y.C.); lfyang@sinh.ac.cn (L.Y.)
†These authors contributed equally to this work.

in skeletal muscles (*20*). Because of the limitation of whole-body deletion of *Slc16a1*, tissue-specific *Slc16a1* knockout mouse models have been recently used to investigate the biological functions of MCT1 in various tissues/cells. Macrophage-specific deletion of *Slc16a1* can prevent M2-like polarization of macrophages, leading to impairment of muscle reperfusion and regeneration from ischemia (*21*). *Slc16a1* deletion in macrophages was also found to affect peripheral nerve regeneration in mice (*22*). *Slc16a1* deficiency in adipocytes stimulated macrophage-mediated inflammation, consequently leading to high-fat diet (HFD)-induced insulin resistance in peripheral tissues (*23*). Hepatic deletion of *Slc16a1* aggravated HFD-induced obesity in female mice but not in male mice (*24*). Deficiency of MCT1 in $CD8^+$ T lymphocytes affects the proliferation and recruitment of the cells to the adipocyte tissues in obesity (*25*). However, deletion of MCT4 was reported to result in exercise intolerance, associated with structural degeneration of the neuromuscular junctions (*25*). In this study, we analyzed a mouse model with specific deletion of *Slc16a1* in skeletal muscle. We discovered that MCT1-mediated lactate shuttle has an active role in promoting mitochondrial biogenesis and TCA flux, in addition to the known function of lactate as an energy fuel to feed the TCA cycle.

RESULTS

Deletion of *Slc16a1* in skeletal muscle increases metabolic rate and improves glucose tolerance in mice

We first explored the capacity of skeletal muscle to metabolize glucose and lactate in vivo. Serum samples were collected from left ventricle and femoral vein of the mice and then analyzed by liquid chromatography–mass spectrometry (fig. S1A). Among the potential fuels that feed TCA cycle, glucose and lactate were the major fuels consumed by skeletal muscle (fig. S1B). Next, we intravenously infused U-^{13}C-glucose or U-^{13}C-lactate and measured their contribution to glycolytic and TCA metabolites (Fig. 1A). Serum and skeletal muscles were collected at pseudo-steady state (2.5 hours after infusion). In theory, intramuscle lactate can be taken in directly from circulation or generated from glucose via glycolysis inside the muscle cells. We found that the normalized ^{13}C level of lactate is higher from ^{13}C-lactate infusion than from ^{13}C-glucose infusion in all the muscle groups tested, including quadriceps (QUA), gastrocnemius (GAS), tibialis anterior (TA), and soleus (SOL) (Fig. 1B). Consequently, skeletal muscles contained more ^{13}C-labeled glycolytic product and TCA metabolites (pyruvate, succinate, and malate) from ^{13}C-lactate than from ^{13}C-glucose (Fig. 1B). We also investigated the direct contribution of these two circulatory nutrients to intramuscle lactate and malate via ^{13}C labeling matrix deconvolution (Fig. 1C and fig. S1C). On the one hand, our analysis revealed that circulatory lactate contributed to ~50% of intramuscle lactate in QUA, TA, and GAS and ~40% of intramuscle lactate in SOL (Fig. 1D). On the other hand, circulatory glucose contributed to <5% of intramuscle lactate in QUA, TA, and GAS and ~20% of intramuscle lactate in SOL (Fig. 1D). Notably, intramuscle malate, a representative TCA metabolite, was exclusively from circulatory lactate in all the muscle groups (Fig. 1D). These results indicate that lactate is the preferred fuel for TCA cycle in skeletal muscle, partly consistent with a previous report (*5*).

Lactate is transported from the circulation to the skeletal muscle via MCTs. Among the 16 MCTs in mammals, MCT1 (*Slc16a1*), MCT2 (*Slc16a7*), and MCT4 (*Slc16a3*) are involved in lactate transport in the skeletal muscle (*1*, *4*). In mice, we found that MCT1 had the highest mRNA level among these three transporters in the skeletal muscle (fig. S1D). Among the four types of skeletal muscles with different oxidation capacity, MCT1 had the highest expression level in SOL, a muscle type with high oxidative capacity, followed by TA, GAS, and QUA, which are mainly fast muscle types with high glycolytic capacity (fig. S1E). Immunofluorescence staining of the skeletal muscle also revealed that MCT1 protein had higher distribution in SOL than in GAS and TA (fig. S1F). These observations are in line with previous findings demonstrating that the expression of MCT1 in individual muscle type is positively correlated with mitochondrial content and oxidation capacity (*1*, *4*, *13*). Also consistent with previous reports, MCT1 was expressed in the membranes of type I, type IIA, and type IIX myofibers while absent in type IIB myofibers that have the highest glycolytic activity among the four major muscle fiber types (Fig. 1E and fig. S1G). Conversely, MCT4 was present in type IIB and IIX fibers but barely detectable in type I and IIA fibers (fig. S1H), consistent with previous reports (*13*, *16*).

As our analysis indicated that MCT1 is the major type of MCTs in the skeletal muscle, we focused our study on MCT1 using a skeletal muscle-specific knockout (mKO) mouse model (Fig. 1F). As expected, the mKO mice expressed little MCT1 in different types of skeletal muscle in comparison with the wild-type (WT) littermates, shown by quantitative real-time polymerase chain reaction (PCR) and immunofluorescence staining (Fig. 1G and fig. S2A). In addition, MCT1 protein level in the plasma membrane and mitochondria fractions was reduced in the skeletal muscle of mKO mice (fig. S2B). In GAS, expressions of both MCT2 and MCT4 were not altered by MCT1 deletion (fig. S2C). In SOL, expression of both MCT2 and MCT4 were reduced by MCT1 deletion (fig. S2C). We also analyzed the protein levels of lactate dehydrogenase A (LDHA), lactate dehydrogenase B (LDHB), and mitochondrial carrier protein 2 (MPC2) using mitochondria fraction from GAS muscle. While LDHA was decreased in mKO mice, LDHB and MPC2 were slightly increased in mKO mice (fig. S2D).

The body weight and lean mass were reduced in mKO mice under normal chow (Fig. 1, H and I). Consistently, we found that the weights of several muscle were reduced in mKO mice (Fig. 1J). Analysis with metabolic cage revealed increases in carbon dioxide production, oxygen consumption, daytime respiratory exchange ratio (RER), and night resting energy expenditure (REE) in mKO mice (Fig. 1K and fig. S2E). The increase in RER might reflect more energy substrate usage from carbohydrate than usage from lipid. To exclude the possibility that the loss of body weight was affected by appetite in mKO mice, we tracked food intake for seven consecutive days, and more food intake was increased in many time points in mKO mice (fig. S2F). In addition, mKO mice had improvement in glucose tolerance (Fig. 1L), while the fasting plasma insulin level and insulin tolerance were not altered (fig. S2, G and H). Collectively, these data indicate that deficiency of MCT1 in skeletal muscle reduces body weight while enhances metabolic rate and improves glucose tolerance in mice.

Deficiency of MCT1 in skeletal muscle elevates intramuscular lactate level, improves running endurance, and switches myofibers toward oxidative type

As MCT1 is a major transporter of lactate, we detected lactate level in the skeletal muscle. Both SOL and QUA had higher lactate level in

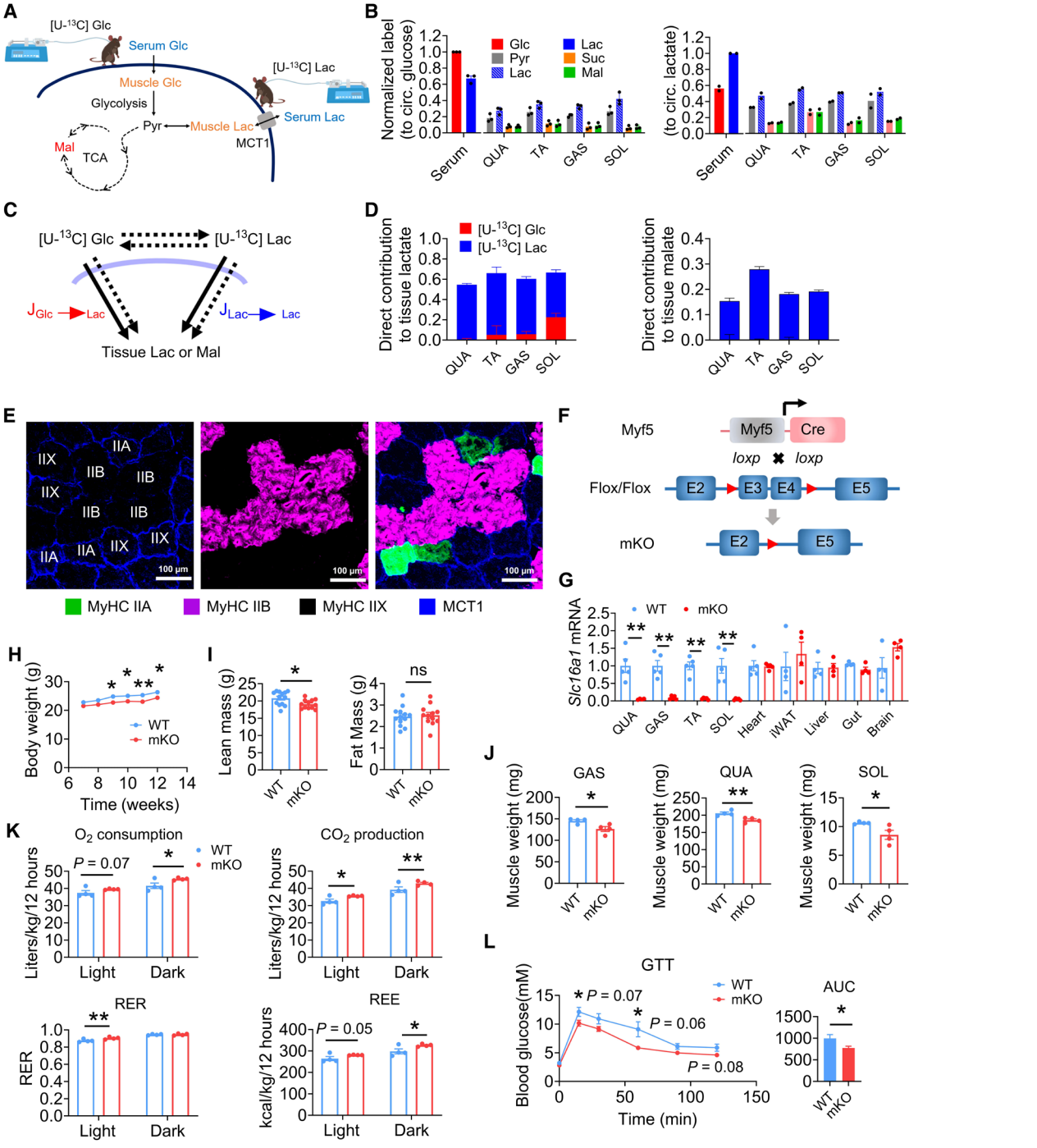

Fig. 1. Metabolic phenotype of mice with deletion of *Slc16a1* in skeletal muscle. (**A**) Schematic showing metabolic pathways of glucose and lactate between blood and skeletal muscle in mice after infusion of [U-^{13}C] glucose or [U-^{13}C] lactate. (**B**) Normalized labeling from 2.5-hour [U-^{13}C] glucose or [U-^{13}C] lactate infusion of glycolytic products in QUA, TA, GAS, and SOL. $n = 2$ to 3. (**C**) Schematic of TCA intermediates, for example, malate, produced from [U-^{13}C] glucose or [U-^{13}C] lactate by jugular vein catheterizing in tissues. (**D**) Direct sources of muscle lactate and malate from circulatory labeled glucose and lactate. $n = 2$ to 3. (**E**) Immunofluorescence staining of MCT1 (blue) with muscle fiber markers for type IIA (green, recognized by anti-MyHC IIA), type IIB (purple, recognized by anti-MyHC IIB), and type IIX (unstained). Scale bars, 100 μm. (**F**) Scheme showing the strategy of generating mouse with *Slc16a1* deletion in skeletal muscle (mKO). (**G**) *Slc16a1* mRNA levels in different tissues of the mice. $n = 5$ for each group. (**H**) Body weight curves of the mice fed with normal chow diet. $n = 10$ to 11 for each group. (**I**) Quantification of body lean mass and fat mass by magnetic resonance imaging. $n = 12$ to 13 for each group. (**J**) Weight of different skeletal muscles. $n = 4$ for each group. (**K**) Results of metabolic cages to quantitate O_2 consumption, CO_2 production, respiratory exchange ratio (RER), and resting energy expenditure (REE) of the mice in light period (7:00 a.m. to 19:00 p.m.) and dark period (19:00 p.m. to 7:00 a.m.). $n = 4$ for each group. (**L**) Glucose tolerance test (GTT) of the mice with corresponding area under curve (AUC). $n = 6$ to 8 for each group. All data are shown as mean ± SEM. $^*P < 0.05$, $^{**}P < 0.01$, and ns for nonsignificant. Glc, glucose; Pyr, pyruvate; Lac, lactate; Citr, citrate; Suc, succinate; Mal, malate.

mKO mice than the WT littermates (Fig. 2A). Moreover, blood lactate level was notably decreased in mKO mice in a treadmill running test (Fig. 2B). Notably, mKO mice had better performance in running endurance when subjected to treadmill for exhausted exercise (Fig. 2C). However, maximal gripping force which mainly tests for the strength of fast glycolytic muscles was reduced in the mKO mice (Fig. 2D).

We next used immunofluorescence staining to determine different types of muscle fibers. mKO mice had a notable increase in the proportion of fast-twitch oxidative IIA fibers, together with a decrease in the proportion of fast-twitch glycolytic IIB fibers in SOL, GAS, and TA (Fig. 2E). It is worth noting that a small percentage of IIB fibers existed in SOL in the WT mice, and these fibers were almost completely disappeared in mKO mice (Fig. 2E and fig. S3A). Highly oxidative type I fibers were almost absent in GAS of the WT mice but started to appear in mKO mice though (Fig. 2E and fig. S3B). In addition to the changes of myofiber composition, a cross-sectional area tended to be reduced in SOL of mKO mice (fig. S3C). Together, these data indicate that loss of MCT1 in skeletal muscle promotes switch of myofibers from glycolytic type to oxidative type. Collectively, these data reveal that loss of MCT1 in skeletal muscle elevates local lactate level, enhances running endurance, and promotes switch of muscle fibers toward oxidative type.

Loss of MCT1 increases glycolytic flux and TCA flux of glucose in the skeletal muscle

To explore the impact of MCT1 deficiency on metabolic flux in skeletal muscle, we used intravenous infusion of ^{13}C-labeled glucose and ^{13}C-labeled lactate to measure their contributions to glycolytic and TCA cycle in the skeletal muscle as described in Fig. 1A. Overall, the contribution of glucose to glycolysis and TCA was increased by MCT1 deletion (Fig. 3A and fig. S4A), while the contribution of lactate was reduced in mKO mice (Fig. 3D and fig. S4B). In particular, the normalized direct contributions of blood glucose to intramuscle lactate and malate were elevated in all the muscle groups tested in

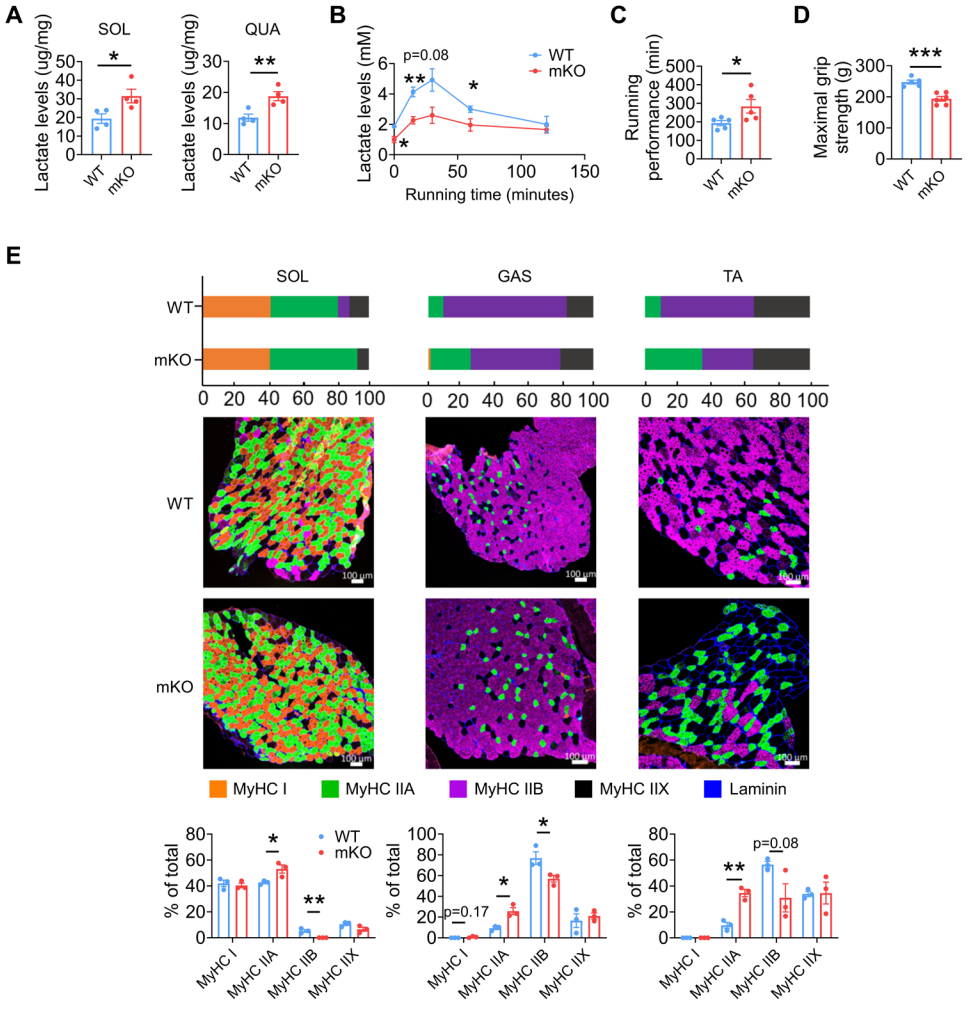

Fig. 2. Deletion of *Slc16a1* in skeletal muscle affects lactate level, improves running performance, and promotes formation of oxidative myofibers. (**A**) Lactate level in SOL and QUA muscles. $n = 4$ for each group. (**B**) Blood lactate level in running mice. $n = 5$ for each group. (**C**) Total running time of exhausted exercise. $n = 5$ for each group. (**D**) Maximal grip strength of the mice. $n = 5$ to 6 for each group. (**E**) Immunofluorescence staining of fiber types in SOL, GAS, and TA muscles. The top histogram represents mean proportions of each type of fibers. The middle are representative immunostaining images for MyHC I (type I, orange), MyHC IIA (type IIA, green), MyHC IIB (type IIB, purple), and MyHC IIX (type IIX, unstained). Laminin (blue) was stained for visualization of the myofiber boundaries. Quantitation of the data is shown in the bottom. Scale bars, 100 μm. $n = 3$ for each group. All data are shown as mean ± SEM. $^*P < 0.05$, $^{**}P < 0.01$, and $^{***}P < 0.001$.

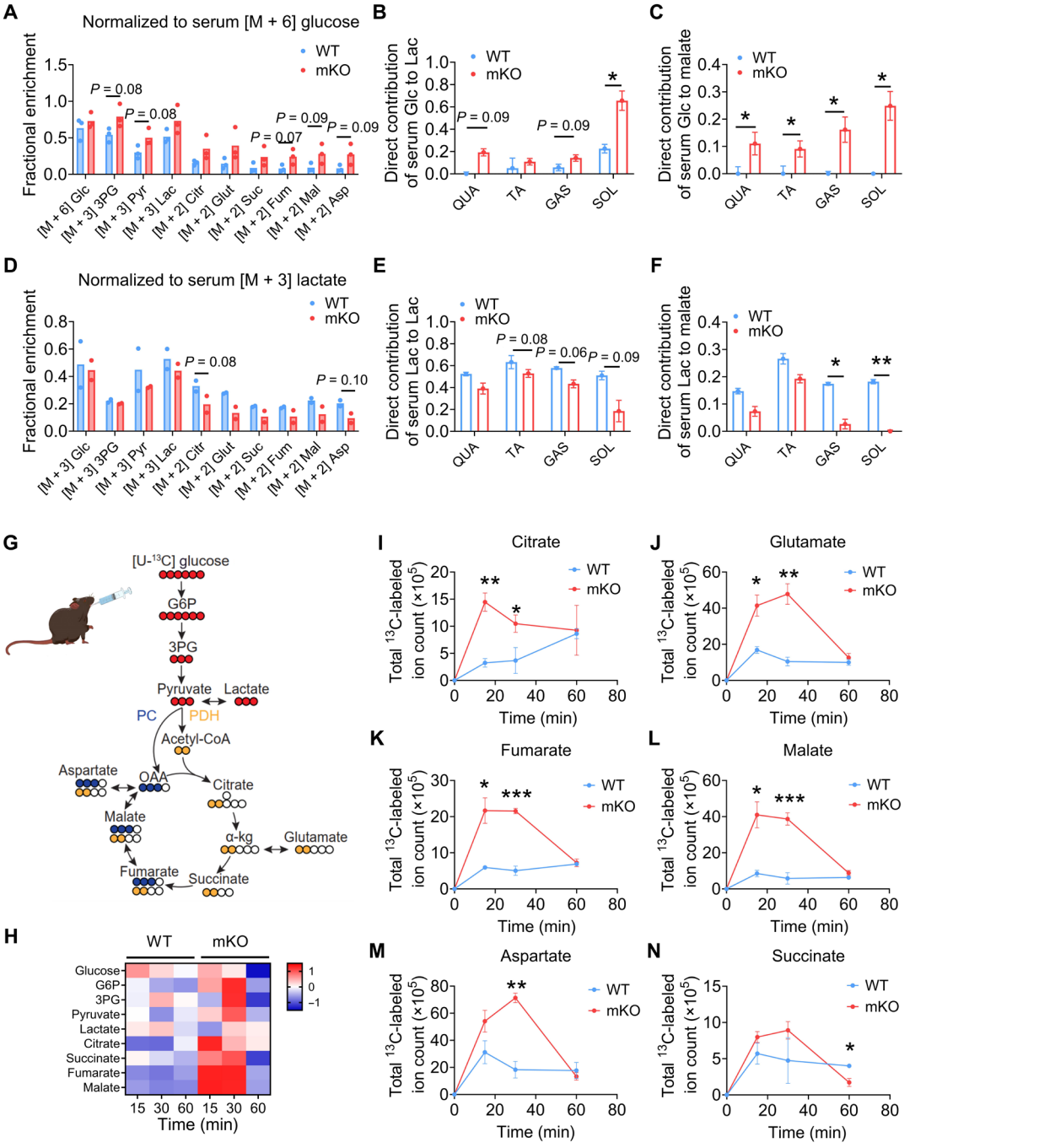

Fig. 3. Deletion of *Slc16a1* in skeletal muscle promotes glycolytic and TCA fluxes of the mice. (**A**) Fractional enrichment of glycolytic and TCA intermediates in SOL muscle after infusion of the tracer, as normalized to serum [U-^{13}C] glucose (with [U-^{13}C] glucose infusion). $n = 3$ for each group. (**B** and **C**) Direct contribution of serum [U-^{13}C] glucose to lactate (B) and malate (C) in different skeletal muscles. $n = 3$ for each group. (**D**) Fractional enrichment of glycolytic and TCA intermediates in SOL muscle after infusion of the tracer, as normalized to [U-^{13}C] lactate (with [U-^{13}C] lactate infusion). $n = 2$ for each group. (**E** and **F**) Direct contribution of serum [U-^{13}C] lactate to lactate (E) and malate (F) of different skeletal muscles. $n = 2$ for each group. (**G**) Schematic of glucose flux via glycolysis and TCA cycle in skeletal muscles via gavaging ^{13}C-labeled glucose. (**H**) Heatmap showing total ^{13}C-labled ion count of major metabolites from glycolysis and TCA cycle in SOL muscle of the mice. $n = 3$ for each group. (**I** to **N**) Total ion counts of ^{13}C-labeled metabolites of TCA cycle in SOL muscle, including citrate (I), glutamate (J), fumarate (K), malate (L), aspartate (M), and succinate (N). $n = 3$ for each group. All data are shown as mean ± SEM. *$P < 0.05$, **$P < 0.01$, and ***$P < 0.001$. Glc, glucose; 3PG, 3-phosphoglycerat; Pyr, pyruvate; Lac, lactate; Citr, citrate; Glut, glutamate; Suc, succinate; Fum, fumarate; Mal, malate; Asp, aspartate.

mKO mice (Fig. 3, B and C). In contrast, direct contributions of blood lactate to intramuscle lactate and malate were reduced when MCT1 was deleted (Fig. 3, E and F).

Considering metabolic diversity among different muscle fibers, we next gavaged ^{13}C-labeled glucose to directly investigate glycolytic and TCA fluxes in the skeletal muscle (Fig. 3G). In SOL, a typical oxidative muscle type, most of the ^{13}C-labeled ion counts of glycolytic and TCA intermediates were increased at 15 and 30 min and dropped at 60 min after the isotope gavage (Fig. 3H). In particular, the TCA intermediates including citrate, malate, fumarate, glutamate, and aspartate were markedly increased at 15 and 30 min after the isotope gavage in mKO mice (Fig. 3, I to M), while succinate level tended to increase at 30 min and decreased at 60 min after the isotope gavage (Fig. 3N). We also observed similar changes of metabolic flux in QUA and GAS muscle groups (fig. S4, C and D). As energy substrate, pyruvate participates in the TCA cycle through pyruvate dehydrogenase (PDH) and pyruvate carboxylase (PC) (fig. S4E). For determination of PDH activity, we detected the ^{13}C-labeled ion counts of [M + 2] citrate, [M + 2] glutamate, and [M + 2] malate at different time points. For PC, we detected the ^{13}C-labeled ion counts of [M + 3] citrate, [M + 3] glutamate, and [M + 3] malate at different time points. As a result, both [M + 2] and [M + 3] intermediates by reactions of PDH and PC were increased at 15 and 30 min after gavage of ^{13}C-labeled glucose in mKO mice (fig. S4, F and G). Collectively, these data indicate that deficiency of MCT1 in skeletal muscle leads to a robustly increased glycolytic flux and TCA flux from glucose.

Inhibition of MCT1 enhances glycolytic and TCA fluxes in C2C12 myotubes

To better understand the impact of MCT1 on glycolysis and TCA metabolism, we blocked MCT1 in vitro with AZD3965, an efficient inhibitor of MCT1 (*26*). Accordingly, we treated differentiated C2C12 cells with ^{13}C-labeled glucose and detected glycolytic and TCA intermediates as well. Inhibition of MCT1 activity by AZD3965 was confirmed by lactate measurement, in which we found that AZD3965 significantly elevated intracellular lactate level while reduced the extracellular lactate level (Fig. 4A).

We first analyzed the effect of blocking MCT1 on the flux of glucose to glycolysis and TCA cycle (Fig. 4B). Inhibition of MCT1 by AZD3965 substantially elevated the glycolytic intermediates and products, including glucose-6-phosphate (G6P), 3-phosphoglycerate (3PG), pyruvate, and lactate in C2C12 myotubes (Fig. 4, B to F). We next examined the activities of PDH and PC by comparing the levels of M + 2 and M + 3 TCA intermediates, respectively, in these cells (Fig. 4, G to Q). Notably, both M + 2 and M + 3 TCA intermediates were elevated upon AZD3965 treatment (Fig. 4, H to M and O to Q). Together, these data indicate that blocking MCT1 promotes glycolytic flux and TCA flux of glucose in C2C12 myotubes.

Deficiency of MCT1 in skeletal muscle promotes biogenesis and function of mitochondria

Both IIA and IIB fibers are fast-twitch muscle fibers, although IIA is fast-twitch oxidative myofiber that has more oxidative capacity than IIB (*27*). Mitochondria abundance is one of the most outstanding distinctions between the two types of fibers. As MCT1 deficiency elevated IIA fibers while decreasing IIB fibers, we hypothesized that MCT1 might affect mitochondria function in the skeletal muscle. We first performed RNA sequencing (RNA-seq) with GAS muscles isolated from mKO and WT mice to analyze changes of gene expression profile. Gene ontology (GO) analysis with all differentially expressed genes (DEGs) revealed enrichment of genes associated with mitochondria functions, such as electron transfer activity, NADH [reduced form of nicotinamide adenine dinucleotide (NAD^+)] dehydrogenase activity, and mitochondrion organization in mKO mice (Fig. 5A). In particular, a plethora of genes related to GO terms of mitochondrion organization and mitochondrial ribosome were up-regulated in mKO muscles (fig. S5, A and B). The set of genes linked to mitochondrial respiratory complex was also elevated in the muscle of mKO mice (Fig. 5B). In line with the changes of gene expression, the protein levels of subunits of mitochondria complexes were up-regulated in the muscle lacking MCT1 (Fig. 5C). Transmission electron microscopy (TEM) analysis revealed a remarkable increase in mitochondria number in MCT1-deleted skeletal muscle, together with a decrease in a cross-sectional area but without change of mitochondria diameter (Fig. 5, D and E). Moreover, mitochondria isolated from GAS of mKO mice exhibited increased oxygen consumption rate (OCR) and respiratory control ratio (Fig. 5F). NADH dehydrogenase activity detected by tetrazolium blue staining in the skeletal muscles was also elevated in the mKO mice (Fig. 5G), further supporting an increase of mitochondrial activity in the skeletal muscle of these mice.

It was known that the number of capillary vessels surrounding slow myofibers is higher than those in fast-twitch fibers (*27*). We found that the capillary density, as determined by anti-CD31 immunostaining, was increased in the skeletal muscle of mKO mice (Fig. 5H). Consistently, CD31 protein level, as well as hypoxia inducible factor 1 alpha subunit (HIF-1α), a key transcriptional factor associated with vascular remodeling, was up-regulated in the skeletal muscle in MCT1-deleted mice (Fig. 5I). Kyoto encyclopedia of genes and genomes (KEGG) enrichment analysis based on all differentially expressed genes also revealed that several pathways, including oxidative phosphorylation, citrate cycle, pyruvate metabolism, and HIF-1 signaling pathway, were increased in the muscle of mKO mice (fig. S5, C and D). In addition, we found that the levels of reactive oxygen species (ROS) and malondialdehyde (MDA) were not altered by MCT1 deletion in the skeletal muscle (fig. S5, E and F), indicating that MCT1 loss does not affect oxidative stress. In sum, these data suggest that muscle-specific MCT1 deficiency can enhance mitochondria biogenesis, mitochondria activity, and capillary density in the skeletal muscle.

Inhibition of MCT1 in C2C12 cells changes myotube morphology and improves mitochondrial function

To gain insight into changes of mitochondrial function in MCT1-depleted muscle, we explored the effect of MCT1 inhibition by AZD3965 on myogenic differentiation of C2C12 cells. We found that AZD3965 promoted myotube formation, shown as an increase in fusion index, increase in myotube length, and decrease in myotube diameter (Fig. 6, A and B), as well as an increase in MyoD mRNA level (Fig. 6C). We next examined how AZD3965 affected muscle fibers in C2C12 myotubes. The mRNA level of the marker for type I oxidative fibers was clearly elevated by AZD3965 (Fig. 6C). At the protein level, markers of type I and type IIA fibers were elevated by AZD3965, while the marker of type IIB fibers was reduced by AZD3965 (Fig. 6D). The expression of genes and proteins of several subunits of the mitochondrial respiratory complex were elevated by AZD3965 treatment in C2C12 myotubes (Fig. 6, E and F). Likewise, gene set

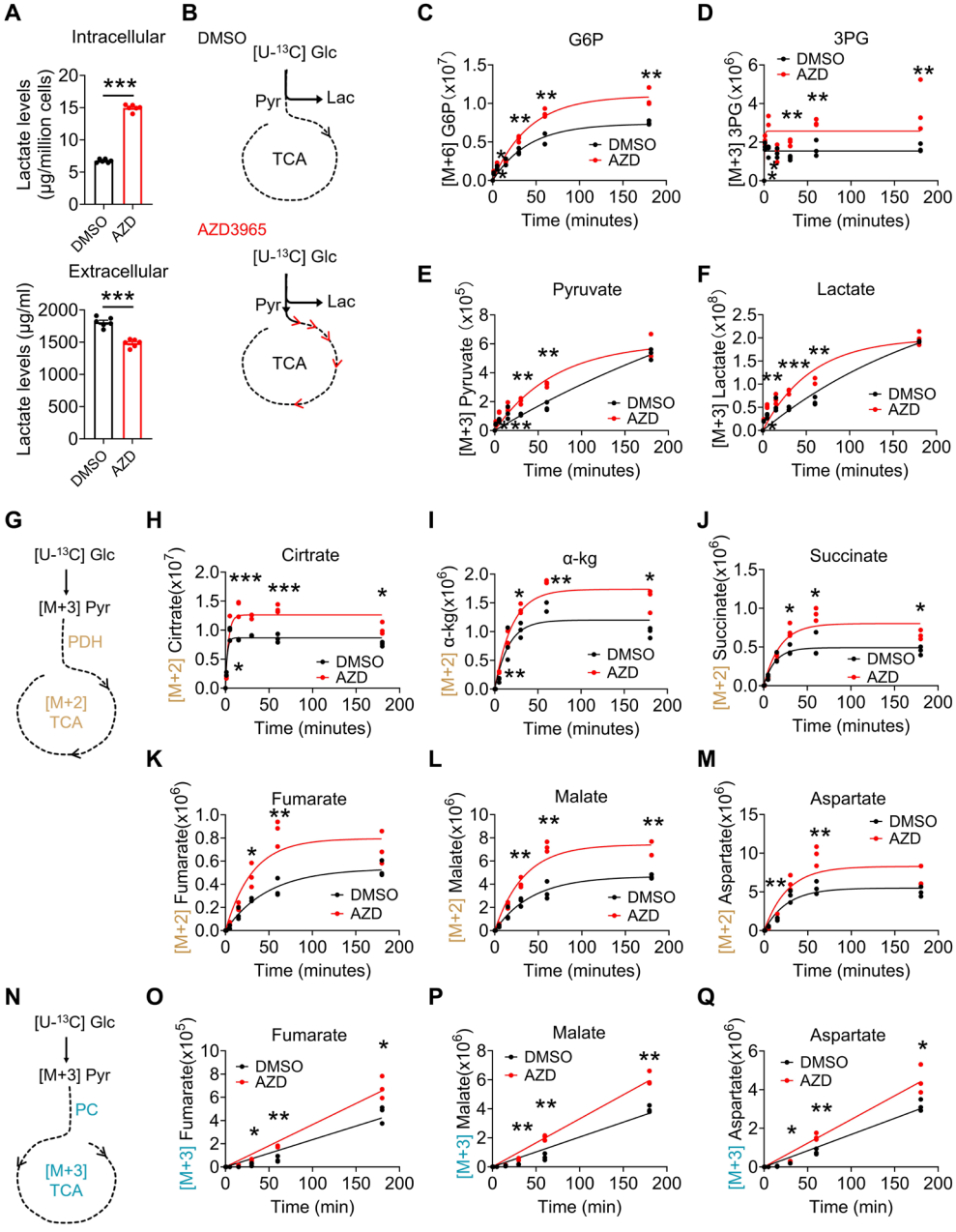

Fig. 4. Inhibition of MCT1 in C2C12 myotubes by AZD3965 enhances glycolytic and TCA fluxes. (**A**) Intracellular and extracellular lactate levels of C2C12 myoblasts treated with 1 μM AZD3965 or 0.1% of dimethyl sulfoxide (DMSO). $n = 6$ for each group. (**B**) Schematic showing metabolic fate of [U-^{13}C] glucose. (**C** to **F**) Total ion counts of [M + 6] and [M + 3] glycolytic intermediates/products from [U-^{13}C] glucose tracing in C2C12 myotubes at different time points. The metabolites include [M + 6] G6P (C), [M + 3] 3PG (D), [M + 3] pyruvate (E), and [M + 3] lactate (F). $n = 3$ for each group. (**G**) Schematic showing metabolic fate of pyruvate originated from [U-^{13}C] glucose in TCA cycle via PDH. (**H** to **M**) Total ion counts of [M + 2] TCA intermediates in C2C12 myotubes, including citrate (H), alpha-ketoglutarate (α-kg) (I), succinate (J), fumarate (K), malate (L), and aspartate (M). $n = 3$ for each group. (**N**) Schematic showing metabolic fate of pyruvate originated from [U-^{13}C] glucose in TCA cycle via PC. (**O** to **Q**) Total ion counts of [M + 3] TCA intermediates, including fumarate (O), malate (P), and aspartate (Q). $n = 3$ for each group. All data are shown as mean ± SEM. *$P < 0.05$, **$P < 0.01$, and ***$P < 0.001$. AZD, AZD3965; Glc, glucose; G6P, glucose-6-phosphate; 3PG, 3-phosphoglycerat; Pyr, pyruvate; Lac, lactate.

enrichment analysis (GSEA) results based on RNA-seq in C2C12 cells revealed a positive correlation of genes related to mitochondrion organization to AZD3965 treatment (Fig. 6G). Moreover, OCR analysis revealed that inhibition of MCT1 elevated basal respiration, maximal respiration, and ATP production in C2C12 myotubes (Fig. 6, H and I), indicating a clear increase in mitochondria activity.

Consistent with the effects of MCT1 inhibitor, similar phenotypes were observed in C2C12 cells with *Slc16a1* knockdown (fig. S6A). Myotubes with *Slc16a1* down-regulation displayed higher fusion index and longer length, together with thinner diameter than the control (fig. S6, B and C). The mRNA levels of MyoD and markers of oxidative fibers were increased by *Slc16a1* knockdown (fig. S6D).

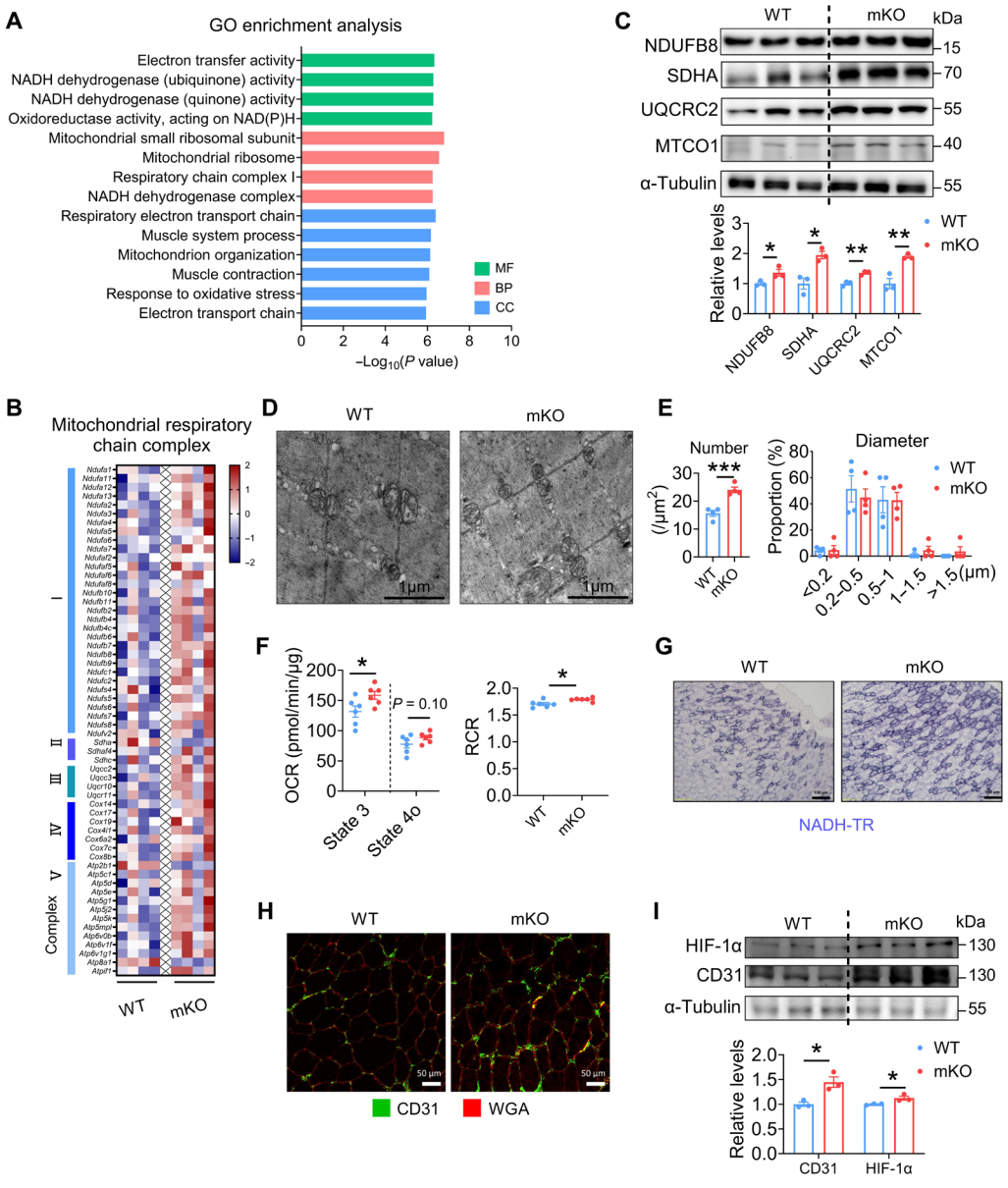

Fig. 5. *Slc16a1*-deleted skeletal muscle has enhanced mitochondrial biogenesis. (**A**) GO enrichment analysis of all differentially expressed genes in GAS muscle between WT and mKO mice. $n = 4$ for each group. BP, biological process; CC, cellular component; MF, molecular function. (**B**) Heatmap of differentially expressed genes related to respiratory complex in GAS muscle. $n = 4$ for each group. (**C**) Immunoblots of representative proteins involved in mitochondrial electron transport chain. Quantitation of the data is shown in the bottom. (**D** and **E**) TEM analysis of GAS muscle. Representative images of TEM are shown in (D), and the calculated number and diameter of the mitochondria are shown in (E). Scale bar, 1 μm. $n = 4$ for each group. (**F**) Analysis of oxidative capacity of isolated mitochondria in GAS from the mice. OCR of isolated mitochondria is shown following the treatment (left). Relative state 3 (adenosine diphosphate–stimulated OCR), state 4o (oligomycin inhibited OCR), as well as the respiratory control ratio (RCR) are indicated (right). $n = 6$ for each group. (**G**) NADH dehydrogenase activity stains in GAS muscles of WT and mKO mice. Scale bars, 100 μm. (**H**) Immunostaining for capillary density using CD31 (green) in TA muscle. Wheat germ agglutinin (WGA; red) was stained for visualization of myofiber boundary. Scale bars, 50 μm. (**I**) Immunoblots of CD31 and HIF-1α. Quantitation of the result is shown on the right. All data are shown as mean ± SEM. $^{*}P < 0.05$, $^{**}P < 0.01$, and $^{***}P < 0.001$.

The protein levels of myosin heavy chain 1 (MyHC I) and the subunits of mitochondria complex were elevated by *Slc16a1* knockdown (fig. S6, E and F). Together, these data demonstrate that inhibition/knockdown of MCT1 in C2C12 myotubes notably influences myotube morphology, promotes muscle fiber switch toward the oxidative type and enhances biogenesis and function of mitochondria.

Deficiency of MCT1 in skeletal muscle or C2C12 cells elevates protein level of PGC-1α

It has been reported that peroxisome proliferator-activated receptor gamma coactivator 1-alpha (PGC-1α), the main regulator of mitochondrial biogenesis, has a lower content in 2B fibers (*28*). Muscle-specific overexpression of PGC-1α displays increased

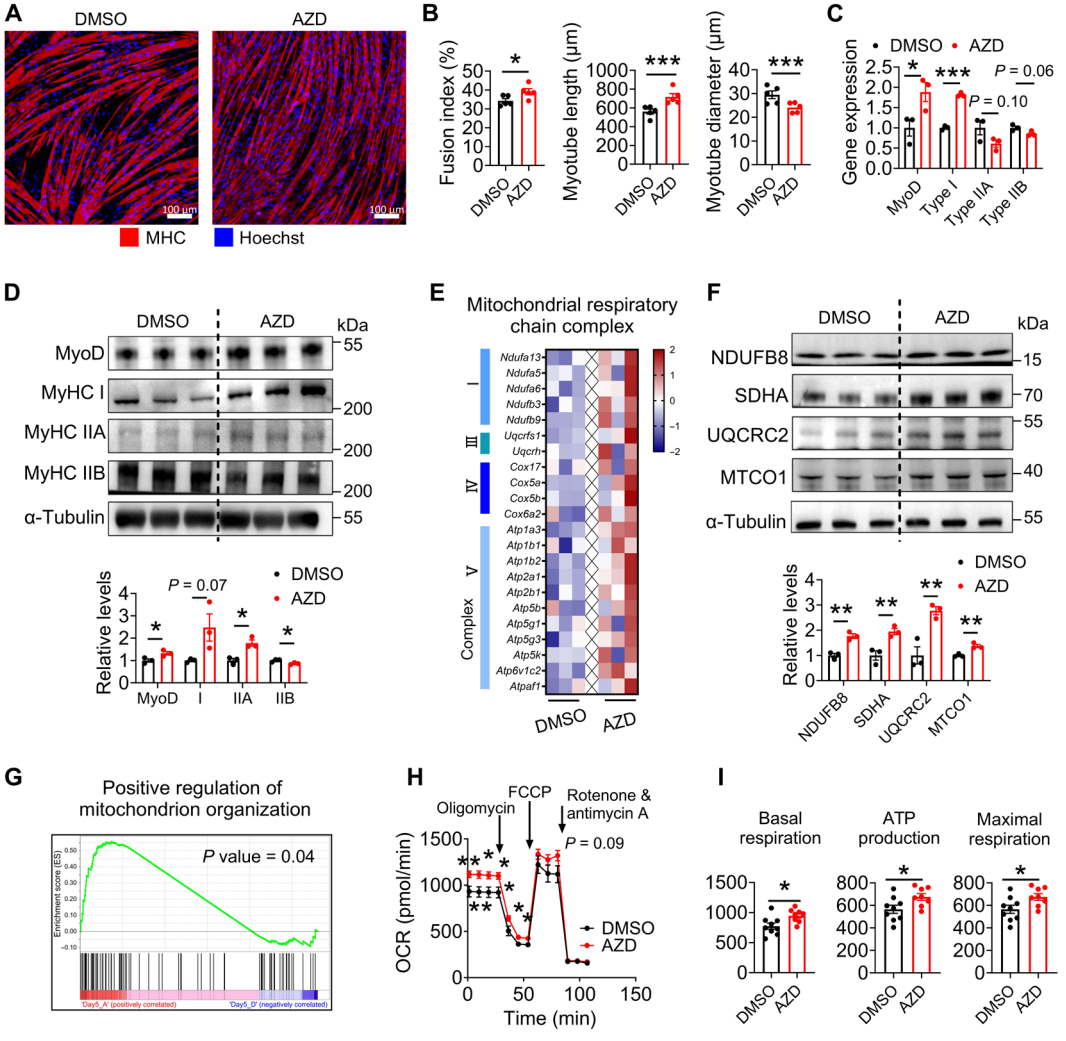

Fig. 6. Inhibition of MCT1 in C2C12 cells improves mitochondrial functions. (**A**) Immunostaining for MHC (red) and nuclei (blue) in differentiated C2C12 cells treated with 1 μM AZD3965 or 0.1% of DMSO. Scale bars, 100 μm. (**B**) Measurement of myotube parameters with the C2C12 myotubes as in (A). $n = 5$ for each group. (**C**) mRNA levels of myotube differentiation marker (MyoD) and isoforms of MyHC in differentiated C2C12 cells. Fiber markers of type I, type IIA, and type IIB are *Myh7*, *Myh2*, and *Myh4*, respectively. $n = 3$ for each group. (**D**) Immunoblots of MyoD and MyHC isoforms in differentiated C2C12 myotubes. Fibers of type I, type IIA, and type IIB were identified antibodies against MyHC I, MyHC IIA, and MyHC IIB, respectively. Quantitation of the result is shown in the bottom. (**E**) Heatmap to show differentially expressed genes of the respiratory complex in differentiated C2C12 cells. $n = 3$ for each group. (**F**) Immunoblots of representative proteins of the respiratory complex in differentiated C2C12 cells. Quantitation of the result is shown in the bottom. (**G**) GSEA of the differentially expressed genes with a GO term "positive regulation of mitochondrion organization." (**H** and **I**) Analysis of oxidative capacity of C2C12 myotubes. OCR is shown following addition of different compounds (H). Basal respiration, ATP production, and maximal respiration are shown individually (I). $n = 8$ to 9 for each group. All data are shown as mean ± SEM. $^*P < 0.05$, $^{**}P < 0.01$, and $^{***}P < 0.001$. AZD, AZD3965.

mitochondrial biogenesis, energy expenditure, oxygen consumption, angiogenesis, and, more remarkably, exercise performance (*29*). We found that the protein level of PGC-1α was notably upregulated in GAS of the mKO mice at both sedentary and running status (Fig. 7, A and B). PGC-1α protein level was also elevated by AZD3965 treatment in C2C12 cells (Fig. 7C). Similarly, knockdown of MCT1 in C2C12 myotubes elevated protein level of PGC-1α (fig. S6F). However, the mRNA level of PGC-1α in both muscle and myoblast displayed no apparent changes (Fig. 7D), indicating that MCT1 deficiency mainly affects PGC-1α at the protein level but not at the transcriptional level.

We next investigated the degradation rate of PGC-1α protein. C2C12 cells were treated with cycloheximide (CHX) to inhibit protein synthesis. Both endogenous and exogenous PGC-1α protein exhibited a reduced degradation rate upon treatment with AZD3965 (Fig. 7, E and F). The half-life of endogenous PGC-1α protein was increased from 10.6 to 19.6 hours by AZD3965 treatment. The half-life of exogenously expressed PGC-1α protein was elevated from 0.4 to 0.5 hours by AZD3965 treatment. Thus, these data suggest that inhibition of MCT1 could increase the PGC-1α protein level via reduction of protein degradation.

We also analyzed whether MCT1 could regulate the activity of PGC-1α protein via NAD-dependent protein deacetylase sirtuin-1 (SIRT1) as it is a key regulator of PGC-1α protein activity (*30*). GSEA results based on RNA-seq in GAS muscle indicated a positive correlation of MCT1 deficiency with genes related to NADH

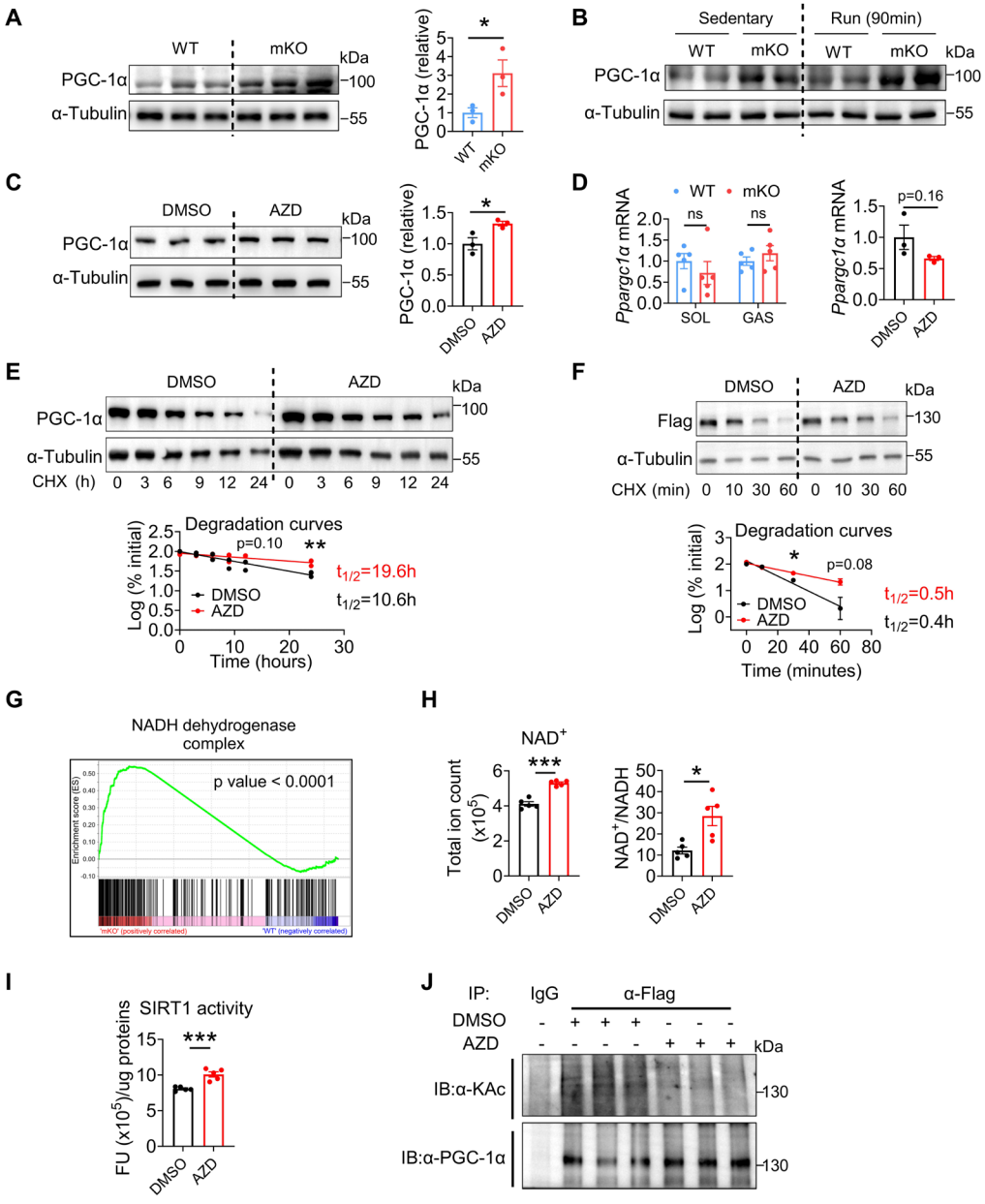

Fig. 7. Elevation of PGC-1α protein by loss/inhibition of MCT1 in skeletal muscle and C2C12 myotubes. (**A**) Immunoblot of PGC-1α in GAS muscle. Quantitation of the result is shown on the right. $n = 3$ for each group. (**B**) Immunoblot of PGC-1α in GAS muscle of the mice under sedentary and running conditions. $n = 2$ for each group. (**C**) Immunoblot of PGC-1α in C2C12 myotubes. Quantitation of the result is shown in the right panel. $n = 3$ for each group. (**D**) *Ppargc1a* mRNA level in mice muscles (left) and C2C12 myotubes (right). (**E**) Degradation rate of endogenous PGC-1α protein in C2C12 myoblasts upon treatment with CHX for different length of times. (**F**) Degradation rate of exogenously expressed PGC-1α protein in C2C12 myoblasts. The pixels for each band were adjusted by α-tubulin. Adjusted data were measured and normalized so that the number of pixels at $t = 0$ was 100%. The $\log_{10}$ value of the percentage of pixels was plotted versus time for each time point, and the half-time ($t_{1/2}$) was calculated from the log of 50% [bottom for (E and F)]. (**G**) GSEA of the differentially expressed genes between WT and mKO GAS muscles with a GO term "NADH dehydrogenase complex." (**H**) NAD^+ level and ratio of NAD^+/NADH in C2C12 myotubes treated with or without AZD3965. (**I**) SIRT1 activity in C2C12mtoblasts treated with or without AZD3965. (**J**) Acetylation of exogenous PGC-1α in C2C12 myoblasts with or without AZD3965 treatment detected by coimmunoprecipitation. IB, immunoblotting; IP, immunoprecipitation. All data are shown as mean ± SEM. $^*P < 0.05$, $^{**}P < 0.01$, and $^{***}P < 0.001$. AZD, AZD3965; CHX, cycloheximide; KAc, lysine acetylation. IgG, immunoglobulin G.

dehydrogenase complex (Fig. 7G). The metabolomic analysis of C2C12 cells showed a significant increase of NAD^+ level and NAD^+/NADH ratio in cells treated with AZD3965 (Fig. 7H). NAD^+ is a substrate activator of SIRT1. Consistently, the enzyme activity of SIRT1 was significantly elevated by AZD3965 treatment in C2C12 cells (Fig. 7I). Acetylation of PGC-1a was reduced by AZD3965 treatment (Fig. 7J). In summary, these data imply that functional deficiency of MCT1 may protect PGC-1α protein from degradation while increase the activity of PGC-1α via NAD^+/SIRT1 signaling pathway, whereby leading to enhancement in mitochondria biogenesis and switch of myofibers to oxidative types.

DISCUSSION

From our findings, in addition to the series of studies conducted by Brooks laboratory (*3*, *4*, *31*), we propose that MCT1-mediated lactate shuttle plays an active role in energy metabolism of the skeletal muscle (Fig. 8). This working model has the following speculations and key features: (i) Different muscle fibers have distinct lactate transporters for cell-cell and intracellular lactate shuttle. MCT4 is mainly expressed in glycolytic muscle fibers (fig. S1H), as previously reported (*13*, *16*). Thus, MCT4 is mainly involved in efflux of lactate from glycolytic muscle fibers. MCT1 is expressed in both plasma membrane and mitochondria in oxidative fibers (Fig. 1E and fig. S2B), consistent with previous reports (*12*–*15*). We also found the lactate level inside mitochondria was decreased upon MCT1 loss (fig. S7) using a mitochondria-localized lactate tracer (*32*). In our model, MCT1 on the plasma membrane of oxidative fibers uptakes lactate released from glycolytic fibers, while MCT1 on the mitochondria membrane transports cytosolic lactate into the mitochondria. This demonstrates that MCT1 is involved in both the cell-cell shuttle and cytosol-mitochondria shuttle of lactate. (ii) Lactate is an important fuel source for the TCA cycle in the mitochondria via MCT1 and mLOC. The K_{eq} of cytosolic LDH is 1000 (*3*), robustly favoring conversion of pyruvate to lactate. In addition, the cytosolic lactate pool is increased by uptake of lactate released from glycolytic fibers via MCT1 on the plasma membrane. The cytosolic lactate is then transported to the mitochondria via MCT1. Inside mitochondria, lactate is quickly oxidized to pyruvate by mitochondrial LDH (mLDH). The presence of LDH in mitochondria was

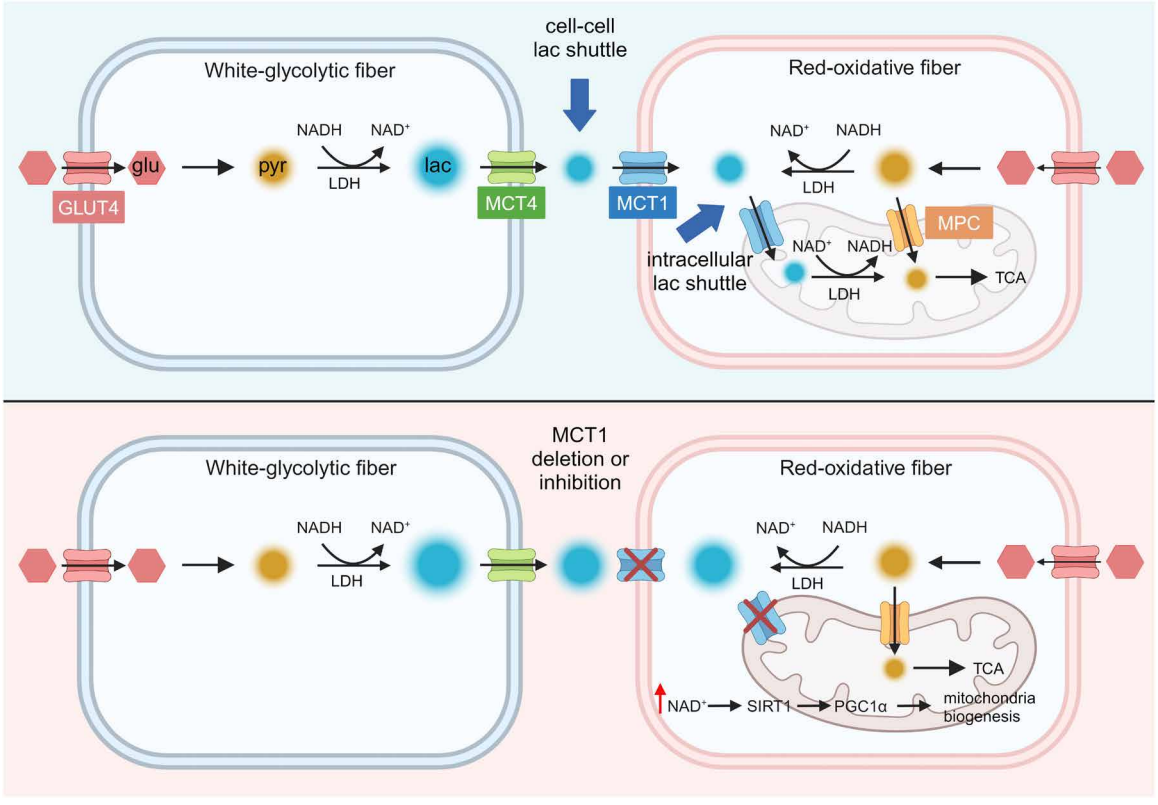

Fig. 8. A working model to depict functions of MCT1 in lactate shuttles in skeletal muscle (generated by BioRender). Different muscle fibers have distinct lactate transporters with MCT4 expressing in glycolytic muscle fibers and MCT1 expressing in both plasma membrane and mitochondria in oxidative fibers. Cell-cell lactate shuttle between glycolytic fibers and oxidative fibers is mediated by MCT4 and MCT1, while cytosol-mitochondria lactate shuttle in oxidative fibers is mediated by MCT1. Lactate is an important fuel source for the TCA cycle in the mitochondria via MCT1 and mLOC in oxidative fibers. Inside mitochondria, lactate is oxidized to pyruvate by mLDH. Intracellular lactate shuttle is important for modulating NAD^+/NADH ratio in the cell. When MCT1 is lost and lactate cannot be shuttled to the mitochondria, conversion of pyruvate to lactate would lead to a net increase of NAD^+, as observed in this study. Intracellular lactate shuttle is linked to the compensatory response of mitochondria biogenesis. When cytosol-mitochondria shuttle of lactate is blocked, the fuel supply from the lactate route is insufficient. The cell would sense the insufficiency of fuel to initiate mitochondria biogenesis for compensation. One mechanism could be the increase of NAD^+ leading activation of SIRT1 and PGC-1α pathway. In addition, lactate shuttle in the skeletal muscle is associated with exercise performance due to its modulation on mitochondria biogenesis. glu, glucose; pyr, pyruvate; lac, lactate; LDH, lactate dehydrogenase; mLDH, mitochondrial lactate dehydrogenase; mLOC, mitochondrial lactate oxidation complex; MPC, mitochondrial pyruvate carrier.

reported previously (*7*) and found in our study (fig. S2D). We propose here that mLDH likely has a kinetic property different from cytosolic LDH, such that mLDH favors flux of lactate to pyruvate. This is a critical question awaiting investigation in the future. (iii) Intracellular lactate shuttle is important for the NAD^+/NADH ratio in the cell. Pyruvate conversion to lactate by LDH in the cytosol would generate equal molar concentration of NAD^+. Conversely, conversion of lactate to pyruvate in the mitochondria would consume equal molar concentration of NAD^+. When MCT1 is lost and lactate cannot be shuttled to the mitochondria, conversion of pyruvate to lactate would lead to a net increase of NAD^+, consistent with our observation (Fig. 7H). (iv) Intracellular lactate shuttle is linked to the compensatory response of mitochondria biogenesis. We postulate that when cytosol-mitochondria shuttle of lactate is blocked, the fuel supply from the lactate route is insufficient. The cell would sense the insufficiency of fuel to initiate mitochondria biogenesis for compensation. Furthermore, the increase of NAD^+ due to loss of MCT1 and inactivity of mLDH would stimulate SIRT1 (Fig. 7, H and I), subsequently leading to deacetylation of PGC-1α (Fig. 7J). It was previously reported that deacetylation of PGC-1α elevates activity of PGC-1α and stimulates mitochondria biogenesis in skeletal muscle in response to fasting (*33*). It is likely that deacetylation of PGC-1α could also reduce degradation of PGC-1α protein as reported in this study (Fig. 7, E and F). (v) Lactate shuttle in the skeletal muscle is associated with exercise performance. In our study, we found that mKO mice had better performance in running endurance (Fig. 2C), with a reduction in maximal gripping force which mainly tests for the strength of fast glycolytic muscles (Fig. 2D). On the basis of our model, MCT1 deletion has a compensatory effect to stimulate mitochondria biogenesis, thus enhancing the mitochondria functions of red oxidative fibers. Lactate released from glycolytic fibers cannot be used by the oxidative fibers due to MCT1 loss, consequently resulting in elevation of intracellular lactate level, inhibition of glycolysis, and activity of glycolytic fibers. (vi) Addition of external lactate cannot stimulate mitochondria function. On the basis of our model, addition of external lactate would be shuttled to the mitochondria and used as a fuel for TCA cycle, leading to a net decrease of NAD^+ level via mLDH. Assuming that an increase of NAD^+/NADH ratio is one of the key driving forces for mitochondria biogenesis, we postulate that the externally added lactate would not lead to increases in mitochondria activity and mitochondrial proteins, as observed in our study (fig. S8), different from the scenario of MCT1 loss/inhibition. It is noteworthy that this is a simplified model in which one cannot rule that low level of lactate shuttle and lactate oxidation occurs in mitochondria of glycolytic fibers and MCT2/MCT4 may mediate part of intracellular lactate shuttle in oxidative fibers.

We observed that glucose tolerance is improved in mKO mice. It is known that the uptake efficiency of energy substrates, such as glucose, lactate, and fatty acids, is higher in oxidative fibers than in glycolytic fibers (*34*–*36*). In addition, the distribution of skeletal muscle fibers may reflect an adaptation to the whole-body metabolism. Reduction of genes related to oxidative metabolism and mitochondrial functions is associated with insulin resistance and type 2 diabetes (*37*). We thus postulate that the improved glucose tolerance in mKO mice is caused by an increase in oxidative myofibers. However, how MCT1 in the skeletal muscle regulates glucose homeostasis needs to be investigated in the future using diet-induced obesity mouse models.

As a key upstream regulator of mitochondrial functions, the functions of PGC-1α in the skeletal muscles have been intensively investigated. Transgenic mice with PGC-1α expression in the skeletal muscle had increased mitochondrial content and oxidative enzymes in oxidative muscle fibers (*29*, *38*). Such phenotype is similar to mKO mice. In our study, we found that deletion or inhibition of MCT1 can increase the protein level of PGC-1α, indicating that the increased mitochondrial biogenesis in the mKO mice is mediated by up-regulation of PGC-1α. The mRNA level of PGC-1α was not altered by MCT1 deletion. Consistently, our data revealed that the protein degradation rate of PGC-1α was reduced by MCT1 inhibition. On the other hand, we found that inhibition of MCT1 was able to elevate intracellular NAD^+ level and stimulate the activity of SIRT1. It has been previously reported that SIRT1 is a key molecule that modulates PGC-1α protein activity (*30*). Therefore, it is likely that the protein level and activity of PGC-1α are both affected by MCT1-mediated lactate transport, thereby contributing to regulation of mitochondrial function. Another possibility is that the lactylation level of PGC-1α protein might affect its protein stability as well as its activity. Lysine lactylation is a novel posttranslational modification that has been found in histones (*10*). Recently, lysine lactylation has been found to be ubiquitous in the human proteome (*39*–*41*). It is thus important to determine in the future whether lysine lactylation of PGC-1α is also involved in the regulation of PGC-1α in the skeletal muscle.

MATERIALS AND METHODS

The sequences of PCR primers are listed in table S1. The catalog numbers of all the reagents are listed in table S2.

Mouse studies

Slc16a1$^{Flox/Flox}$ mice were obtained from Shanghai Model Organisms Center (Shanghai, China) as previously described (*23*). Myf5-cre mice, purchased from the Jackson Laboratory, were gifts of Y. Hao from Shanghai Institute of Nutrition and Health (SINH), Chinese Academy of Sciences (CAS). All mouse strains are on the C57BL/6 genetic background. For specific deletion of *Slc16a1* gene in skeletal muscle, *Slc16a1*$^{Flox/Flox}$ mice were crossed with Myf5-cre mice to generate mKO mice. The mice were genotyped by a PCR method using genomic DNA isolated from the tails. Genotyping of the mice expressing *Slc16a1* alleles with floxed site was performed with primers 5′-TGTACCAGCCACCGTCCTT-3′ and 5′-CATCTTGCCTGAGCGTCTAA-3′. Genotyping of mice expressing Myf5-cre was performed with primers provided on the website of the Jackson Laboratory (https://jax.org/). *Slc16a1*$^{Flox/Flox}$ (WT) and mKO littermates aged 5 to 6 weeks were fed with normal chow diet. Mice were maintained in specific pathogen–free facility and kept on a 12-hour light/dark cycle with free access to food and water. All the mouse studies were performed in male mice. All animal experimental protocols were approved by Institutional Animal Care and Use Committee Institutional Animal Care and Use Committee of Shanghai Institute of Nutrition and Health, CAS with an approval number SINH-2020-CY-1.

Exhausted exercise

Mouse treadmill exercise experiments were performed as previously described with minor modifications (*42*). Briefly, mice were acclimated to treadmill (Columbus Instruments) for 2 days. On

day 1, mice ran for 5 min at a speed of 5 m/min followed by 2 min at a speed of 8 m/min. On day 2, mice ran for 5 min at a speed of 8 m/min followed by 2 min at a speed of 10 m/min. On day 3, mice were allowed to rest. For exhausted exercise, on day 4, food was removed from the mouse cages for 4 hours before the mice were subjected to adaptive period with a gradually increasing speed from 0 to 10 m/min followed by the exhaustion run at 10 m/min till the mice failed. Blood glucose and lactate levels were measured using a glucometer (Bayer) and a Lactate Scout analyzer (EKF Diagnostic) with tail-nip bleeding. Tissues were snap-frozen using liquid nitrogen, and serum or plasma was obtained at desired time points after exercise.

Grip test

Muscle strength was measured by pulling the mouse backward with a continuous movement after the mouse held firmly to the grip of a strength meter (YLS-13A, Guide Chem). The test was repeated twice, with 5 min between tests. The maximal grip strength from each mouse was collected.

Body composition and metabolic cage analyses

The body composition of the mice was assessed by EchoMRI (Houston). The data of total body fat mass and lean mass were collected for each mouse according to manufacturer's directions. For metabolic cage analysis, the mice were randomly chosen for determination of metabolic rate using the comprehensive laboratory animal monitoring system (CLAMS-16, Columbus Instruments) according to the manufacturer's instructions. Mice were allowed to acclimate to the system for the first 24 hours, and the data were collected for the next 48 hours. Oxygen uptake (VO_2), carbon dioxide production (VCO_2), and RER were recorded. REE was calculated by Weir equation $REE(kcal/day) = [(3.94 \times VO_2) + (1.1 \times VCO_2)] \times 1.44$. All the parameters were collected every 16 min.

Glucose tolerance test and insulin tolerance test

For glucose tolerance test, the mice were fasted overnight for 16 hours and subsequently given glucose solution (1 g/kg; Sigma-Aldrich) by intraperitoneal injection. For insulin tolerance test, the mice were fasted for 4 hours and subsequently injected intraperitoneally with insulin solution (1 U/kg; Novo Nordisk). Blood glucose was determined from tail vein at 0, 15, 30, 60, 90, and 120 min after glucose or insulin administration using a glucometer (Bayer).

Cell culture

C2C12 cells were cultured in [Dulbecco's Modified Eagle Medium (DMEM) (Gibco) supplemented with 10% fetal bovine serum (FBS) (Gibco) and 1% penicillin-streptomycin] and differentiated in differentiation medium [DMEM (Gibco) supplemented with 2% donor horse serum (Biological Industries) and 1% penicillin-streptomycin] in a humidified incubator with 5% CO_2 and 95% air at 37°C. For the AZD3965 treatment, the medium containing 1 μM AZD3965 was changed every day to make sure that MCT1 was continuously inhibited.

Lentivirus

For knockdown of *Slc16a1*, the 5′-3′ sequence of short hairpin RNA (shRNA) is CCAGTGAAGTATCATGGATATCTCGAGATATCCATGATACTTCACTGG. The 5′-3′ sequence of blank control shRNA is TTCTCCGAACGTGTCACGT. Lentivirus [LV3 (H1/GFP and Puro)] consisted of shRNA was purchased from GenePharm Technology. Transduction of lentivirus was conducted as the manufacturer's instructions. Cells stably knockdown of MCT1 were enriched by puromycin selection for positive clones. For overexpression of PGC-1α in C2C12 cells, overexpressed lentivirus (pcSLenti-EF1-EGFP-CMV-Ppargc1a-3xFLAG-WPRE) and the blank control (pcSLenti-EF1-EGFP-CMV-MCS-3xFLAG-WPRE) were purchased from Obio Technology. Transduction of lentivirus was conducted as per the manufacturer's instruction. Cells stably expressing PGC-1α-3 × Flag were enriched by puromycin selection for positive clones.

SIRT1 activity assay

SIRT1 activity was measured with a SIRT1 fluorimetric activity assay kit (CS1040, Sigma-Aldrich) according to the manufacturer's protocol. Fluorescence intensities were measured with a microplate fluorometer (excitation wavelength, 360 nm; emission wavelength, 450 nm).

Transcriptome analysis with skeletal muscle and C2C12 cells via RNA-seq

For RNA extraction, the mouse muscle tissues and C2C12 cells were frozen in liquid nitrogen and stored at −80°C. Total RNA was isolated from these samples using TRIzol reagent (Invitrogen) according to the manufacturer's instructions, and genomic DNA was removed using deoxyribonuclease I (Takara). RNA quality [RNA integrity number (RIN)] was determined by a Agilent 2100 Bioanalyzer (Agilent). RNA concentration was determined by a NanoDrop 2000 (Thermo Fisher Scientific), and the integrity was also examined by agarose gel electrophoresis. Only high-quality RNA samples [optical density (OD) 260/280 = 1.8 to 2.2, OD 260/230 ≥ 2.0, RIN ≥ 6.5] were used to construct sequencing library. The transcriptome library was prepared following the TruSeq RNA sample preparation Kit from Illumina (Illumina) using 1 μg of total RNA. Shortly, mRNA was isolated according to a polyA selection method by oligo(dT) beads and then fragmented at fragmentation buffer. The double-stranded cDNA was synthesized using a SuperScript double-stranded cDNA synthesis kit (Invitrogen) with random hexamer primers (Illumina). Then, the synthesized cDNA was subjected to end-repair, phosphorylation, and "A" base addition according to the Illumina's library construction protocol. Libraries were size-selected for cDNA target fragments of 300 bp on 2% Low Range Ultra Agarose (Bio-Rad, USA) followed by PCR amplification using Phusion DNA polymerase (New England Biolabs) for 15 cycles. After quantification by TBS380, paired-end RNA-seq sequencing library was sequenced with the Illumina HiSeq X ten/NovaSeq 6000 sequencer (2 × 150 bp read length). The raw paired end reads were trimmed and quality-controlled by SeqPrep (version 1.2; https://github.com/jstjohn/SeqPrep) and Sickle (version 1.3.3; https://github.com/najoshi/sickle) with default parameters. Then, clean reads were separately aligned to reference genome of *Mus musculus* (GRCm38.p6) with orientation mode using HISAT2 (version 2.2.1; http://ccb.jhu.edu/software/hisat2/index.shtml) (*43*) software. The mapped reads of each sample were assembled by StringTie (version 2.2.0; https://ccb.jhu.edu/software/stringtie/index.shtml?t=example) in a reference-based approach (*44*). The transcriptome data were analyzed on the online platform of Majorbio Cloud Platform (https://majorbio.com). To identify DEGs (differential expression transcripts) between two different groups, the expression level of each transcript was calculated according to the transcripts per million reads method. RNA-Seq by

Expectation-Maximization (version 1.3.3; http://deweylab.biostat.wisc.edu/rsem/) (*45*) was used to quantify gene abundances. In particular, differential expression analysis was performed using the EdgeR (*46*) with P value < 0.05, and DEGs with fold change > 1 were considered to be significantly different expressed transcripts. GO functional enrichment and KEGG pathway analysis were carried out by Goatools (version 1.3.11; https://github.com/tanghaibao/Goatools) and Python scipy software (version 1.9.0; https://scipy.org/install/).

Immunofluorescence staining

Muscles were mounted at resting length in optimal cutting temperature medium (Tissue-Tek) and snap-frozen in thawing isopentane for ~1 min before transfer to liquid nitrogen and storage at −80°C. Muscle sections (4 μm) were cut at −20°C on a cryostat (Leica), collected on SuperFrost Plus (Thermo Fisher Scientific) adhesion slides, and stored at −80°C. Frozen muscle section slides were equilibrated at room temperature for 15 min and rehydrated in phosphate-buffered saline (PBS) for 15 min. For fiber typing, sections were blocked and permeabilized in blocking buffer containing 5% of goat serum and 0.4% of Triton X-100 in PBS for 1 hour. Primary antibodies were diluted in blocking buffer, and incubation was performed overnight at 4°C. Incubation with secondary antibodies, diluted in blocking buffer, was performed at room temperature for 1 hour. Fiber typing was performed with Development Studies Hybridoma Bank (DSHB) mouse monoclonal antibodies for MyHC I (BA-D5), MyHC IIA (SC71), and MyHC IIB (BF-F3), as previously described (*47*). Fiber boundaries were costained with an anti-laminin antibody (L9393, Merck), and MCT1 was stained with anti-MCT1 antibody (A3013, Abclonal). After incubation in primary antibodies, sections were washed 5 min in PBS for three times and then incubated in a secondary antibody solution containing DyLight 405 (35551, Invitrogen), Alexa Fluor 568 (A-21144, Invitrogen), Alexa Fluor 488 (A-21121, Invitrogen), and Alexa Fluor 647 (A-21238, Invitrogen) in blocking buffer. Sections were then washed 5 min in PBS for three times and mounted with Fluoromount (F4680, Sigma-Aldrich). For visualization of blood vessels, the sections were stained with anti-CD31 antibody (AF3628, R&D Systems). To facilitate visualization of fiber boundaries, glycosaminoglycans in the extracellular matrix were stained with Texas Red–conjugated wheat germ agglutinin (W21405, Invitrogen). Nuclear staining was performed with Hoechst 33342 (H3570, Invitrogen). For myotubes, the cells were seeded in a 24-well glass bottom plate (P24-1.5H-N, Cellvis). After treatment, the cells were fixed in 4% formaldehyde for 10 min at room temperature and permeabilized in PBS with 0.2% of Triton X-100 for 10 min and blocked in 5% of goat serum for 1 hour at room temperature. Last, the samples were incubated overnight at 4°C with mouse anti-MHC (MF20, DSHB) and subsequently incubated with Alexa Fluor 568 (A-21144, Invitrogen). Fusion index was measured with the ratio of nuclei number in myotubes and all nuclei number in a visual field. More than three photos were taken for each sample. Mean fusion index, myotube length, and myotube diameter were calculated on the basis of two to three visual fields, and the mean values from each biological replicate were used for statistical analysis. Quantifications of the proportions of myofibers and parameters of myotubes were measured by ImageJ.

Mitochondrial lactate measurement

For mitochondrial lactate quantification in C2C12 myoblasts, cells were seeded in a 24-well glass bottom plate (P24-1.5H-N, Cellvis). The cells were transfected with a mitochondria-localized fluorescent lactate probe (*32*). The cells were then treated with dimethyl sulfoxide (DMSO), AZD3965, and SL (sodium lactate; 20 mM) for 30 min before image acquirement. As for the group of AZD + SL, we first treated cells with AZD3965 for 30 min and then change the medium with both AZD39665 plus SL. All pictures captured were under the same parameters. Quantifications of the fluorescence signals were measured by ImageJ.

Staining of NADH dehydrogenase activity

NADH dehydrogenase activity was measured by NADH nitrotetrazolium blue staining. Frozen sections were incubated with freshly prepared NADH-nitrotetrazolium blue (NTB) solution [1.5 mM NADH, 1.5 mM NTB, and 0.2 M tris-HCl (pH 7.4)] for 20 min at 37°C. Sections were washed with deionized water, dehydrated in graded ethanol, cleared in xylene, and mounted with Fluoromount (F4680, Sigma-Aldrich).

Measurement of oxygen consumption

For Seahorse analysis (XF24, Agilent Technologies), C2C12 myoblasts were seeded at a density of 2×10^4 per well cultured in XF24 plates. After differentiation for 4 days, the culture mediums were changed with fresh prepared assay solution according to protocols supplied by Agilent Technologies (https://agilent.com.cn). Cells were then subjected to the machine to measure OCR with sequential supplementation with oligomycin (final concentration, 1 μM), carbonyl cyanide *p*-trifluoromethoxyphenylhydrazone (FCCP; final concentration, 2 μM), and rotenone/antimycin A (final concentration, 0.75 μM).

Mitochondrial isolation and measurement of OCR

Mitochondria were isolated from freshly dissected GAS muscle using a mitochondrial isolation kit [HY-K1061, MedChemExpress (MCE)]. Mitochondrial protein concentration was measured using an Enhanced BCA Protein Assay Kit (P0009, Beyotime). Oxygen consumption measurement was performed in a Seahorse XF24 instrument as described previously (*48*). Briefly, 2 to 3 μg of freshly isolated mitochondria was added to each well in mitochondrial isolation buffer [20 mM Hepes, 70 mM sucrose, 220 mM mannitol, 1 mM EGTA, 10 mM KH_2PO_4, and 5 mM $MgCl_2$ (pH7.2)] in a Seahorse XF24 plate and pelleted by 15 min of centrifugation at 4°C at the speed of 3000*g*. Mitochondria were then subjected to the machine to measure OCR with sequential injections of adenosine diphosphate (final concentration, 4 mM), oligomycin (final concentration, 2 μM), FCCP (final concentration, 4 μM), and antimycin A (final concentration, 4 μM).

Isolation of plasma membrane and mitochondria

Before membrane protein extraction, skeletal muscle was digested as single-cell suspension using collagenase. Then, we used a Membrane and Cytosol Protein Extraction Kit (P0033, Beyotime) to perform membrane protein isolation. Mitochondria were isolated from freshly dissected skeletal muscle using a mitochondrial isolation kit (HY-K1061, MCE). Fresh isolated mitochondria were lysed and boiled in SDS sample buffer. The supernatant was able to be subjected to immunoblotting analysis.

ROS and MDA assays

ROS level in skeletal muscle was conducted using an ROS assay kit (#E-BC-K138-F, Elabscience). Before testing, skeletal muscle was digested as single-cell suspension using collagenase. About 10^4 to 10^6

cells were subjected to ROS measurement with a microplate fluorometer, and the results were adjusted by protein concentration. MDA was detected using an MDA assay kit (S0131S, Beyotime). Briefly, TA muscles were cut into scraps as small as possible and lysed by radioimmunoprecipitation assay lysis buffer (MA0151, meilunbio). After centrifugation at 12,000*g* and 4°C for 10 min, the supernatant was subjected to the test according to the product instruction, and the results were adjusted by protein concentration.

Western blotting analysis

Mouse tissues were lysed with RIPA lysis buffer (MA0151, meilunbio) with protease and phosphatase inhibitors. Cell cultures were washed with PBS and collected by SDS lysis buffer [125 mM tris-HCl (pH6.8), 2% SDS, and 10% glycerol] with protease and phosphatase inhibitor cocktails. Protein concentrations were determined by the Enhanced BCA Protein Assay Kit (P0009, Beyotime). The samples were subjected to SDS–polyacrylamide gel electrophoresis on 10% running gels, transferred to polyvinylidene fluoride membranes, and incubated with 3% bovine serum albumin in TBST (tris-buffered saline, 0.1% Tween 20) at room temperature for 1 hour. The membrane was then incubated with primary antibodies. The antibodies used were as follows: MyHC I (BA-D5, DSHB), MyHC IIA (SC71, DSHB), MyHC IIB (BF-F3, DSHB), CD31 (PECAM-1, AF3628, R&D Systems), HIF-1α (21691, Antibodies & Bioreagents Manufacturer), NDUFB8 (ab192878, abcam), SDHA (ab14715, abcam), UQCRC1 (ab110252, abcam), UQCRC2 (ab203832, abcam), MTCO1 (ab14705, abcam), MyoD (sc-377460, Santa Cruz), MHC (MF20, DSHB), PGC-1α (A20995, Abclonal), MCT1 (A3013, Abclonal), Flag (F3165, Sigma-Aldrich), LDHA (A1146, Abclonal), LDHB (A18096, Abclonal), MPC2 (A20196, Abclonal), adenosine triphosphatase (T40109, Abmart), TOM20 (11802-1-AP, Proteintech), acetylated lysine (#9441, Cell Signaling Technology), and α-tubulin (T6074, Sigma-Aldrich) overnight at 4°C. After incubation with specific secondary antibody, the membranes were visualized via the SuperSignal West Dura Extended Duration Substrate (Thermo Fisher Scientific) and the Western blot imaging system (Tanon). Quantifications of intensities of the bands in Western blots were measured by ImageJ.

Quantitative real-time PCR

Total RNA was extracted from tissue samples or cultured cells using TRIzol reagent (Invitrogen). cDNA was synthesized from 1 μg of total RNA using the FastKing RT Kit (with gDNase) (TIANGEN Biotech). Quantitative real-time PCR primer sequences are included in table S1. The relative expression levels of genes were normalized to their corresponding *Actb* or 18*S* ribosomal RNA level.

Measurement of lactate in skeletal muscle and myoblast

The method of muscle specimen isolation and analyte extraction was described as previously reported (*49*). For culture cells, ~6×10^5 myoblasts per well were first washed with PBS and then homogenized in 1-ml solution mixed with 40% methanol, 40% acetonitrile, and 20% deionized water followed by centrifugation at 12,500 rpm and 4°C for 10 min. The clear supernatant isolated from tissue and cells was transferred to a 1.5-ml microtube and diluted into appropriate concentration. All the samples were optimized by the reaction of derivatization using 3-NPH as described by Han *et al* (*49*). At the end of derivatization, a 5-μl aliquot of each solution was injected for liquid chromatography–tandem mass spectrometry (LC-MS/MS) analysis.

Sample preparation and metabolite extraction for LC-MS

Serum samples were collected from left ventricle and femoral vein (for analysis of major nutrients by skeletal muscle) or from tail vein during anesthesia. The mice were fasted for 5 hours before infusion. Mice were anesthetized with isoflurane and euthanized by cervical dislocation. The blood samples were kept on ice. After centrifugation (at 14,000 rpm at 4°C for 10 min), serum was collected and stored in −80°C till extraction. Three microliters of serum was mixed with 120 μl of 100% methanol, vortexed sufficiently, and centrifuged twice for 30 min each at 4°C, 14000 rpm. Then, the supernatant was used in LC-MS analysis. Tissue samples were clamped (by Wollenberger clamp) into liquid nitrogen immediately after cervical dislocation of mice and stored at −80°C. Frozen tissues were pulverized using a Cryomill (Retsch); 10 to 20 mg of the resulting powder was weighed into a precooled tube and mixed well with 40% of methanol, 40% of acetonitrile, and 20% of water with 0.5% of formic acid (40 μl of solvent per mg tissue) at −20°C. After sufficient vortex, 15% of NH_4HCO_3 solution [8.5% (v/v) of extraction buffer] was added to neutralize formic acid. Samples were centrifuged twice for 30 min each at 4°C, and the supernatant were transferred for LC-MS analysis. For C2C12 cells, the culture medium was replaced with fresh DMEM (10% of dialyzed FBS and 1% of penicillin-streptomycin) with 25 mM [U-^{13}C] glucose. Cell samples were collected at corresponding time points. Medium was aspirated, and cells were washed with cold PBS immediately to remove remaining medium. Then, extraction buffer (−20°C, 40% of methanol, 40% of acetonitrile, and 20% of water with 0.5% of formic acid) was directly added into a 6- or 12-well plate (120 μl of solvent per 1,000,000 cells). Then, cells were scraped on ice, and samples were transferred into 1.5-ml tubes, following by neutralization with 15% of NH_4HCO_3 solution [8.5% (v/v) of extraction buffer]. After centrifugation twice (4°C, 14,000 rpm, 30 min) to remove cell debris, the supernatant was used for LC-MS analysis.

LC-MS method

To measure the absolute concentrations of pyruvate and lactate, the Agilent 1200 high performance LC system (Agilent Technologies, USA), coupled to a 4000Q TRAP triple quadrupole mass spectrometer (AB Sciex, USA) equipped with a Turbo Ion Spray source, was used. Chromatographic separation was performed on a Waters XBridge C18 (2.1 mm by 150 mm, 3.5 μm) high-performance liquid chromatography column, using 0.01% formic acid in water (solvent A) and acetonitrile with 0.01% formic acid (solvent B) as the mobile phase for binary gradient elution. The column flow rate was 0.2 ml/min, the column temperature was 40°C, and the autosampler was kept at 4°C. The binary elution gradient was 20% B to 95% B in 7 min and then maintained at 95% B for 5 min. The column was equilibrated for 7 min with the initial solvent composition between injections. The negative ion multiple reaction monitoring (MRM) transitions for each targeted analyte were optimized via flow injection analysis of a solution prepared from 3-NPH derivatization of lactate and pyruvate mixed standard solution. At least two MRM transitions (Q1/Q3) per analyte were obtained [lactate: 224.1/152.0 mass/charge ratio (*m/z*); pyruvate: 357.1/150.0 *m/z*].

The electrospray ionization mass spectrometry parameters were the ion spray voltage, −4500 V; nebulizer gas (N2), 50 U; curtain gas (N2), 15 U; collision gas (N2), medium; entrance potential, −10 V; and collision cell exit potential, −5 V. The drying gas (N2) flow and temperature were 50 U and 500°C, respectively. The Q1

and Q3 operations were set to unit resolution. LC-MS/MS data were acquired using the Analyst 1.6 software and were processed using the MultiQuant 3.0 software (AB Sciex, USA).

To detect isotope-labeled products from ^{13}C tracing, Q-Exactive Plus obitrap mass spectrometry and a Vanquish Ultra Performance Liquid Chromatography system (Thermo Fisher Scientific) were used. The temperature of Hilic column (2.1 mm × 150 mm, 5 μm; HILICON) was maintained at 25°C during analysis. Solvent A is 95% of water and 5% of acetonitrile with 20 mM ammonium acetate and 20 mM ammonium hydroxide at pH 9.4, and solvent B is acetonitrile. The gradient was 0 to 2 min, 95% B; 3 to 7 min, 75% B; 8 to 9 min, 70% B; 10 to 12 min, 50% B; 13 to 14 min, 25% B; 16 to 20.5 min, 0% B; and 21 to 28 min, 90% B. Injection volume was 5 μl. The Q-Exactive Plus mass spectrometer was operated in switching negative/positive ion mode scanning from *m/z* 60 to 900 with a resolution of 140,000 at *m/z* 200 (AGC target 3e6, Maximum IT 200 ms). LC-MS data were acquired and analyzed by El-Maven, followed by natural abundance correction via isoCor.

In vivo [U-^{13}C]-glucose gavage tracing

Mice were fasted overnight from 5:00 p.m. (day 0) to 9:00 a.m. (day 1), and blood samples (~20 μl) were collected by tail bleeding for 0 min time point. Then, mice were gavaged with water containing [U-^{13}C] glucose [1 mg/g, body weight (10 μl/g); CLM-1396-PK, Cambridge Isotope Laboratories]. After 15, 30, and 60 min, mice were anesthetized with isoflurane and euthanized by cervical dislocation. Blood samples (~100 μl) were collected from heart puncture, and tissue samples were clamped for sample preparation and analysis.

In vivo isotope infusion

Mouse jugular vein catheterization surgery was performed 1 week before infusion for [U-^{13}C] glucose and [U-^{13}C] lactate (CLM-1579-PK, Cambridge Isotope Laboratories) tracing. Infusion was performed for 2.5 hours to achieve isotopic pseudo-steady state. The infusion setup included a tether and swivel system, connecting to the button pre-implanted under the back skin of mice. Mice were fasted from 10:00 a.m. to 3 p.m. and infused from 3 p.m. till 5:30 p.m. [U-^{13}C] glucose (300 mM) was dissolved in saline, or 435 mM [U-^{13}C] SL was prepared in water. Infusates were infused via the catheter at a constant rate (0.1 μl/min per g mouse weight) using a syringe pump. At the end of infusion, mice were euthanized by cervical dislocation. Blood and tissue samples were then collected.

Data analysis

Definition of normalized labeling

At steady state, the fraction of the mass isotopomer $[M + i]$ of the nutrient in samples is measured as $L_{[M+i]}$ (i is from 0 to N). L is the fraction of labeled carbon atoms in the nutrient, defined as

$$L = \frac{\sum_{i=0}^{N} i \cdot L_{[M+i]}}{N}$$

With the infusion of a ^{13}C-labeled tracer X, the normalized labeling of the downstream metabolites Y is defined as

$$L_{Y \leftarrow X} = \frac{L_Y}{L_X}$$

Calculation of direct contributions with the constraint of non-negative values

As described by Hui *et al.* (*50*), we aimed to determine the direct contribution of glucose and lactate to the tissue lactate and TCA cycle by constructing a set of linear equations. As defined above, the normalized TCA labeling in tissue from circulating metabolites X ($L_{\mathrm{TCA} \leftarrow X}$) as the normalized labeling of tissue lactate or malate to serum X ^{13}C fractional labeling. Because of the interconversion of glucose and lactate, the measured TCA labeling from X can be summed with (direct contribution to TCA from nutrient X) * (1) and (direct contribution to TCA from nutrient Y) * [normalized labeling of Y with X as tracer ($L_{Y \leftarrow X}$)]. Similar calculation applies to TCA labeling from Y. Consequently, we can generate the linear equations

$$\begin{pmatrix} 1 & L_{\mathrm{lac}\leftarrow\mathrm{glc}} \\ L_{\mathrm{glc}\leftarrow\mathrm{lac}} & 1 \end{pmatrix} \cdot \begin{pmatrix} f_{\mathrm{TCA}\leftarrow\mathrm{glc}} \\ f_{\mathrm{TCA}\leftarrow\mathrm{lac}} \end{pmatrix} = \begin{pmatrix} L_{\mathrm{TCA}\leftarrow\mathrm{glc}} \\ L_{\mathrm{TCA}\leftarrow\mathrm{lac}} \end{pmatrix}$$

Transmission electron microscopy

Four-month-old mice were euthanized, and muscles were surgically excised, trimmed to small pieces, and immediately immersed in cold 2.5% of glutaraldehyde. Muscles were further processed for electron microscopy. Briefly, tissue was cut into small pieces and fixed in 2.5% of glutaraldehyde in 0.1 M sodium phosphate buffer (pH 7.4) overnight at 4°C. Subsequently samples were rinsed with the same buffer and postfixed in 2% of osmium tetroxide in 0.1 M sodium phosphate buffer for 1.5 hours at room temperature. After three times of rinsing steps in double distilled water, samples were lastly dehydrated in ethanol and embedded in Epon. Seventy-nanometer sections were poststained with 2% of uranyl acetate and Reynolds lead citrate. Sections were examined with a FEI Tecnai G2 Spirit operated at 120 kV. Images were acquired using a Ganta charge-coupled device camera. Quantifications of mitochondrial number and diameter were measured by ImageJ.

Statistical analysis

Data are expressed as mean ± SEM. Unpaired Student's *t* test with two tails was used to determine the significance of the differences between two groups. One-way analysis of variance (ANOVA) was performed for comparisons among more than two groups with a false discovery rate (FDR) post hoc analysis. To determine whether two different factors have an effect on a measured variable, a two-way ANOVA was used, followed by an FDR post hoc test. Statistical tests were performed using Microsoft Excel (Microsoft) or Prism 9 (GraphPad Software).

Supplementary Materials

This PDF file includes:

Figs. S1 to S8

Tables S1 and S2

REFERENCES AND NOTES

1. B. S. Ferguson, M. J. Rogatzki, M. L. Goodwin, D. A. Kane, Z. Rightmire, L. B. Gladden, Lactate metabolism: Historical context, prior misinterpretations, and current understanding. *Eur. J. Appl. Physiol.* **118**, 691–728 (2018).
2. G. A. Brooks, The lactate shuttle during exercise and recovery. *Med. Sci. Sports Exerc.* **18**, 360–368 (1986).
3. G. A. Brooks, The science and translation of lactate shuttle theory. *Cell Metab.* **27**, 757–785 (2018).
4. G. A. Brooks, J. A. Arevalo, A. D. Osmond, R. G. Leija, C. C. Curl, A. P. Tovar, Lactate in contemporary biology: A phoenix risen. *J. Physiol.* **600**, 1229–1251 (2022).

5. S. Hui, J. M. Ghergurovich, R. J. Morscher, C. Jang, X. Teng, W. Lu, L. A. Esparza, T. Reya, Z. Le, J. Yanxiang Guo, E. White, J. D. Rabinowitz, Glucose feeds the TCA cycle via circulating lactate. *Nature* **551**, 115–118 (2017).
6. J. D. Rabinowitz, S. Enerback, Lactate: The ugly duckling of energy metabolism. *Nat. Metab.* **2**, 566–571 (2020).
7. G. A. Brooks, H. Dubouchaud, M. Brown, J. P. Sicurello, C. E. Butz, Role of mitochondrial lactate dehydrogenase and lactate oxidation in the intracellular lactate shuttle. *Proc. Natl. Acad. Sci. U.S.A.* **96**, 1129–1134 (1999).
8. T. Hashimoto, G. A. Brooks, Mitochondrial lactate oxidation complex and an adaptive role for lactate production. *Med. Sci. Sports Exerc.* **40**, 486–494 (2008).
9. K. Ahmed, S. Tunaru, C. Tang, M. Muller, A. Gille, A. Sassmann, J. Hanson, S. Offermanns, An autocrine lactate loop mediates insulin-dependent inhibition of lipolysis through GPR81. *Cell Metab.* **11**, 311–319 (2010).
10. D. Zhang, Z. Tang, H. Huang, G. Zhou, C. Cui, Y. Weng, W. Liu, S. Kim, S. Lee, M. Perez-Neut, J. Ding, D. Czyz, R. Hu, Z. Ye, M. He, Y. G. Zheng, H. A. Shuman, L. Dai, B. Ren, R. G. Roeder, L. Becker, Y. Zhao, Metabolic regulation of gene expression by histone lactylation. *Nature* **574**, 575–580 (2019).
11. A. P. Halestrap, M. C. Wilson, The monocarboxylate transporter family—Role and regulation. *IUBMB Life* **64**, 109–119 (2012).
12. C. K. Garcia, J. L. Goldstein, R. K. Pathak, R. G. Anderson, M. S. Brown, Molecular characterization of a membrane transporter for lactate, pyruvate, and other monocarboxylates: Implications for the Cori cycle. *Cell* **76**, 865–873 (1994).
13. T. Hashimoto, S. Masuda, S. Taguchi, G. A. Brooks, Immunohistochemical analysis of MCT1, MCT2 and MCT4 expression in rat plantaris muscle. *J. Physiol.* **567**, 121–129 (2005).
14. N. Merezhinskaya, W. N. Fishbein, Monocarboxylate transporters: Past, present, and future. *Histol. Histopathol.* **24**, 243–264 (2009).
15. G. A. Brooks, M. A. Brown, C. E. Butz, J. P. Sicurello, H. Dubouchaud, Cardiac and skeletal muscle mitochondria have a monocarboxylate transporter MCT1. *J. Appl. Physiol.* **87**, 1713–1718 (1999).
16. C. Juel, A. P. Halestrap, Lactate transport in skeletal muscle - role and regulation of the monocarboxylate transporter. *J. Physiol.* **517**, 633–642 (1999).
17. V. N. Jackson, N. T. Price, L. Carpenter, A. P. Halestrap, Cloning of the monocarboxylate transporter isoform MCT2 from rat testis provides evidence that expression in tissues is species-specific and may involve post-transcriptional regulation. *Biochem. J.* **324**, 447–453 (1997).
18. P. M. van Hasselt, S. Ferdinandusse, G. R. Monroe, J. P. Ruiter, M. Turkenburg, M. J. Geerlings, K. Duran, M. Harakalova, B. van der Zwaag, A. A. Monavari, I. Okur, M. J. Sharrard, M. Cleary, N. O'Connell, V. Walker, M. E. Rubio-Gozalbo, M. C. de Vries, G. Visser, R. H. Houwen, J. J. van der Smagt, N. M. Verhoeven-Duif, R. J. Wanders, G. van Haaften, Monocarboxylate transporter 1 deficiency and ketone utilization. *N. Engl. J. Med.* **371**, 1900–1907 (2014).
19. S. Lengacher, T. Nehiri-Sitayeb, N. Steiner, L. Carneiro, C. Favrod, F. Preitner, B. Thorens, J. C. Stehle, L. Dix, F. Pralong, P. J. Magistretti, L. Pellerin, Resistance to diet-induced obesity and associated metabolic perturbations in haploinsufficient monocarboxylate transporter 1 mice. *PLOS ONE* **8**, e82505 (2013).
20. B. Chatel, D. Bendahan, C. Hourde, L. Pellerin, S. Lengacher, P. Magistretti, Y. Le Fur, C. Vilmen, M. Bernard, L. A. Messonnier, Role of MCT1 and CAII in skeletal muscle pH homeostasis, energetics, and function: In vivo insights from MCT1 haploinsufficient mice. *FASEB J.* **31**, 2562–2575 (2017).
21. J. Zhang, J. Muri, G. Fitzgerald, T. Gorski, R. Gianni-Barrera, E. Masschelein, G. D'Hulst, P. Gilardoni, G. Turiel, Z. Fan, T. Wang, M. Planque, P. Carmeliet, L. Pellerin, C. Wolfrum, S. M. Fendt, A. Banfi, C. Stockmann, I. Soro-Arnaiz, M. Kopf, K. De Bock, Endothelial lactate controls muscle regeneration from ischemia by inducing M2-like macrophage polarization. *Cell Metab.* **31**, 1136–1153.e7 (2020).
22. M. K. Jha, J. V. Passero, A. Rawat, X. H. Ament, F. Yang, S. Vidensky, S. L. Collins, M. R. Horton, A. Hoke, G. A. Rutter, A. Latremoliere, J. D. Rothstein, B. M. Morrison, Macrophage monocarboxylate transporter 1 promotes peripheral nerve regeneration after injury in mice. *J. Clin. Invest.* **131**, e141964 (2021).
23. Y. Lin, M. Bai, S. Wang, L. Chen, Z. Li, C. Li, P. Cao, Y. Chen, Lactate is a key mediator that links obesity to insulin resistance via modulating cytokine production from adipose tissue. *Diabetes* **71**, 637–652 (2022).
24. X. Luo, Z. Li, L. Chen, X. Zhang, X. Zhu, Z. Wang, Y. Chen, Monocarboxylate transporter 1 in the liver modulates high-fat diet-induced obesity and hepatic steatosis in mice. *Metabolism* **143**, 155537 (2023).
25. C. Macchi, A. Moregola, M. F. Greco, M. Svecla, F. Bonacina, S. Dhup, R. K. Dadhich, M. Audano, P. Sonveaux, C. Mauro, N. Mitro, M. Ruscica, G. D. Norata, Monocarboxylate transporter 1 deficiency impacts $CD8^+$ T lymphocytes proliferation and recruitment to adipose tissue during obesity. *iScience* **25**, 104435 (2022).
26. R. Polanski, C. L. Hodgkinson, A. Fusi, D. Nonaka, L. Priest, P. Kelly, F. Trapani, P. W. Bishop, A. White, S. E. Critchlow, P. D. Smith, F. Blackhall, C. Dive, C. J. Morrow, Activity of the monocarboxylate transporter 1 inhibitor AZD3965 in small cell lung cancer. *Clin. Cancer Res.* **20**, 926–937 (2014).
27. S. Schiaffino, C. Reggiani, Fiber types in mammalian skeletal muscles. *Physiol. Rev.* **91**, 1447–1531 (2011).
28. M. Sandri, J. Lin, C. Handschin, W. Yang, Z. P. Arany, S. H. Lecker, A. L. Goldberg, B. M. Spiegelman, PGC-1alpha protects skeletal muscle from atrophy by suppressing FoxO3 action and atrophy-specific gene transcription. *Proc. Natl. Acad. Sci. U.S.A.* **103**, 16260–16265 (2006).
29. J. Lin, H. Wu, P. T. Tarr, C. Y. Zhang, Z. Wu, O. Boss, L. F. Michael, P. Puigserver, E. Isotani, E. N. Olson, B. B. Lowell, R. Bassel-Duby, B. M. Spiegelman, Transcriptional co-activator PGC-1α drives the formation of slow-twitch muscle fibres. *Nature* **418**, 797–801 (2002).
30. M. Lagouge, C. Argmann, Z. Gerhart-Hines, H. Meziane, C. Lerin, F. Daussin, N. Messadeq, J. Milne, P. Lambert, P. Elliott, B. Geny, M. Laakso, P. Puigserver, J. Auwerx, Resveratrol improves mitochondrial function and protects against metabolic disease by activating SIRT1 and PGC-1alpha. *Cell* **127**, 1109–1122 (2006).
31. G. A. Brooks, C. C. Curl, R. G. Leija, A. D. Osmond, J. J. Duong, J. A. Arevalo, Tracing the lactate shuttle to the mitochondrial reticulum. *Exp. Mol. Med.* **54**, 1332–1347 (2022).
32. X. Li, Y. Zhang, L. Xu, A. Wang, Y. Zou, T. Li, L. Huang, W. Chen, S. Liu, K. Jiang, X. Zhang, D. Wang, L. Zhang, Z. Zhang, Z. Zhang, X. Chen, W. Jia, A. Zhao, X. Yan, H. Zhou, L. Zhu, X. Ma, Z. Ju, W. Jia, C. Wang, J. Loscalzo, Y. Yang, Y. Zhao, Ultrasensitive sensors reveal the spatiotemporal landscape of lactate metabolism in physiology and disease. *Cell Metab.* **35**, 200–211.e9 (2023).
33. Z. Gerhart-Hines, J. T. Rodgers, O. Bare, C. Lerin, S. H. Kim, R. Mostoslavsky, F. W. Alt, Z. Wu, P. Puigserver, Metabolic control of muscle mitochondrial function and fatty acid oxidation through SIRT1/PGC-1alpha. *EMBO J.* **26**, 1913–1923 (2007).
34. E. W. Kraegen, J. A. Sowden, M. B. Halstead, P. W. Clark, K. J. Rodnick, D. J. Chisholm, D. E. James, Glucose transporters andin vivoglucose uptake in skeletal and cardiac muscle: Fasting, insulin stimulation and immunoisolation studies of GLUT1 and GLUT4. *Biochem. J.* **295**, 287–293 (1993).
35. C. Juel, H. Pilegaard, Lactate/H+ transport kinetics in rat skeletal muscle related to fibre type and changes in transport capacity. *Pflugers Arch.* **436**, 560–564 (1998).
36. A. Chabowski, J. C. Chatham, N. N. Tandon, J. Calles-Escandon, J. F. Glatz, J. J. Luiken, A. Bonen, Fatty acid transport and FAT/CD36 are increased in red but not in white skeletal muscle of ZDF rats. *Am. J. Physiol. Endocrinol. Metab.* **291**, E675–E682 (2006).
37. M. E. Patti, A. J. Butte, S. Crunkhorn, K. Cusi, R. Berria, S. Kashyap, Y. Miyazaki, I. Kohane, M. Costello, R. Saccone, E. J. Landaker, A. B. Goldfine, E. Mun, R. DeFronzo, J. Finlayson, C. R. Kahn, L. J. Mandarino, Coordinated reduction of genes of oxidative metabolism in humans with insulin resistance and diabetes: Potential role of PGC1 and NRF1. *Proc. Natl. Acad. Sci. U.S.A.* **100**, 8466–8471 (2003).
38. S. Miura, Y. Kai, M. Ono, O. Ezaki, Overexpression of peroxisome proliferator-activated receptor gamma coactivator-1alpha down-regulates GLUT4 mRNA in skeletal muscles. *J. Biol. Chem.* **278**, 31385–31390 (2003).
39. N. Wan, N. Wang, S. Yu, H. Zhang, S. Tang, D. Wang, W. Lu, H. Li, D. G. Delafield, Y. Kong, X. Wang, C. Shao, L. Lv, G. Wang, R. Tan, N. Wang, H. Hao, H. Ye, Cyclic immonium ion of lactyllysine reveals widespread lactylation in the human proteome. *Nat. Methods* **19**, 854–864 (2022).
40. J. Wang, P. Yang, T. Yu, M. Gao, D. Liu, J. Zhang, C. Lu, X. Chen, X. Zhang, Y. Liu, Lactylation of PKM2 suppresses inflammatory metabolic adaptation in pro-inflammatory macrophages. *Int. J. Biol. Sci.* **18**, 6210–6225 (2022).
41. K. Yang, M. Fan, X. Wang, J. Xu, Y. Wang, F. Tu, P. S. Gill, T. Ha, L. Liu, D. L. Williams, C. Li, Lactate promotes macrophage HMGB1 lactylation, acetylation, and exosomal release in polymicrobial sepsis. *Cell Death Differ.* **29**, 133–146 (2022).
42. D. A. Sliter, J. Martinez, L. Hao, X. Chen, N. Sun, T. D. Fischer, J. L. Burman, Y. Li, Z. Zhang, D. P. Narendra, H. Cai, M. Borsche, C. Klein, R. J. Youle, Parkin and PINK1 mitigate STING-induced inflammation. *Nature* **561**, 258–262 (2018).
43. D. Kim, B. Langmead, S. L. Salzberg, HISAT: A fast spliced aligner with low memory requirements. *Nat. Methods* **12**, 357–360 (2015).
44. M. Pertea, G. M. Pertea, C. M. Antonescu, T. C. Chang, J. T. Mendell, S. L. Salzberg, StringTie enables improved reconstruction of a transcriptome from RNA-seq reads. *Nat. Biotechnol.* **33**, 290–295 (2015).
45. B. Li, C. N. Dewey, RSEM: Accurate transcript quantification from RNA-Seq data with or without a reference genome. *BMC Bioinformatics* **12**, 323 (2011).
46. M. D. Robinson, D. J. McCarthy, G. K. Smyth, edgeR: A Bioconductor package for differential expression analysis of digital gene expression data. *Bioinformatics* **26**, 139–140 (2010).
47. K. A. Dyar, S. Ciciliot, L. E. Wright, R. S. Bienso, G. M. Tagliazucchi, V. R. Patel, M. Forcato, M. I. Paz, A. Gudiksen, F. Solagna, M. Albiero, I. Moretti, K. L. Eckel-Mahan, P. Baldi, P. Sassone-Corsi, R. Rizzuto, S. Bicciato, H. Pilegaard, B. Blaauw, S. Schiaffino, Muscle insulin sensitivity and glucose metabolism are controlled by the intrinsic muscle clock. *Mol. Metab.* **3**, 29–41 (2014).
48. Z. Chen, B. Bordieanu, R. Kesavan, N. P. Lesner, S. S. K. Venigalla, S. D. Shelton, R. J. DeBerardinis, P. Mishra, Lactate metabolism is essential in early-onset mitochondrial myopathy. *Sci. Adv.* **9**, eadd3216 (2023).

49. J. Han, S. Gagnon, T. Eckle, C. H. Borchers, Metabolomic analysis of key central carbon metabolism carboxylic acids as their 3-nitrophenylhydrazones by UPLC/ESI-MS. *Electrophoresis* **34**, 2891–2900 (2013).
50. S. Hui, A. J. Cowan, X. Zeng, L. Yang, T. TeSlaa, X. Li, C. Bartman, Z. Zhang, C. Jang, L. Wang, W. Lu, J. Rojas, J. Baur, J. D. Rabinowitz, Quantitative fluxomics of circulating metabolites. *Cell Metab.* **32**, 676–688.e4 (2020).

Acknowledgments: We thank all the staff in the institutional animal facility of the Shanghai Institute of Nutrition and Health (SINH), Chinese Academy of Sciences for the careful management of the experimental animals, especially during the outbreak of COVID-19 pandemic in 2020. We thank J. Zhang at Northeast Electric Power University for cartoon drawing. We thank S. Chen at WGU Labs, South Salt Lake, UT for editorial assistance. **Funding:** This study was funded by the National Key Research and Development Program of China (2023YFA1801100 to Y.C. and SQ2022YFA1300091 to L.Y.), National Natural Science Foundation of China (32230047 to Y.C. and 32271354 to L.Y.), and Shanghai Municipal Science and Technology Major Project (to Y.C.). **Author contributions:** Conceptualization: Y.C., L.Z., and L.Y. Data curation: L.Z. and C.X. Formal analysis: L.Z. and C.X. Methodology: L.Z., Y.C., and L.Y. Investigation: L.Z., C.X., S.W., S.Z., J.Z., Z.L., and Y.L. Visualization: L.Z. Supervision: Y.C., L.Y., and L.Z. Writing—original draft: L.Z., Y.C., S.W., L.Y., and C.X. Writing—review and editing: Y.C., L.Z., and L.Y. Validation: Y.C., L.Z., and L.Y. **Competing interests:** The authors declare that they have no competing interests. **Data and materials availability:** All data needed to evaluate the conclusions in the paper are present in the paper and/or the Supplementary Materials. The RNA-seq data have been deposited in the NCBI Sequence Read Archive (SRA) database with accession number PRJNA1013718.

Submitted 11 December 2023
Accepted 17 May 2024
Published 26 June 2024
10.1126/sciadv.adn4508